DIPLOMARBEIT

Titel der Diplomarbeit

„A study of vibration induced distortion on the output current of photovoltaic solar modules“

Verfasser

Julian Schmid

angestrebter akademischer Grad

Magister der Naturwissenschaften (Mag. rer.nat)

Wien, Oktober 2012

Contents

Contents

Acknowledgment

My thanks go to Ass. Prof. Viktor Schlosser, for suggesting this diploma thesis and greatly supporting me during its genesis.

Further I want to thank my family, friends and colleagues.

Finally a big thank-you goes to my parents for their relentless support.

1. Motivation

In the decade from 2000 until 2010 the global installed cumulative photovoltaic capacity rose from 1.5 GW to 39.5 GW, with an increase of 7.2 GW in 2010 alone [2]. With this steady growth of photovoltaic systems and the ongoing trend towards large scale grid connected power stations, new challenges in assuring power quality arise [7, 8]. This has invoked numerous investigations about the proper interfacing such preserving power quality and avoiding electromagnetic interference [9, 10].

However only little research has been done so far in the study of distortion caused by the power generator itself which is transmitted to the subsequent electric conditioning system [26, 30]. As yet the research focus clearly lies on dealing with the symptoms of distortion, rather than looking at its causes. Thus making it very hard, to avoid any unwanted effects during the planning and design of PV stations beforehand.

Beside the intrinsic noise of the photovoltaic cells numerous external sources can introduce current transients, spikes and oscillations as illustrated by figure 1.1.

These noise sources cover a wide frequency range from below 1 Hz typical for cloud movements [16] up to 10 GHz which is caused by satellite communication channels.

Although the externally introduced current noise at the terminals of a single module may not exceed several mA in amplitude electrical interconnections of an assembly of modules summarizes the noise amplitudes which are conducted to the power conditioning unit.

Current transients in the low to very low frequency regime are extremely hard to remove in the circuitry by a low pass filter without the reduction of the useful d.c. output.

Because of the need to optimize the exposure of solar modules to the incident sun light they are placed on mounting constructions which easily are stimulated to vibrate. These vibrations cause changes of the module's surface orientation with respect to the incident sun rays. As a consequence light intensity oscillations cause current oscillations at the module's output.

In space applications scientists are aware of this problem and efforts were undertaken to reduce the vibrations transmitted from the satellite to the solar array paddles [20]. For terrestrial photovoltaic applications the resonance frequency
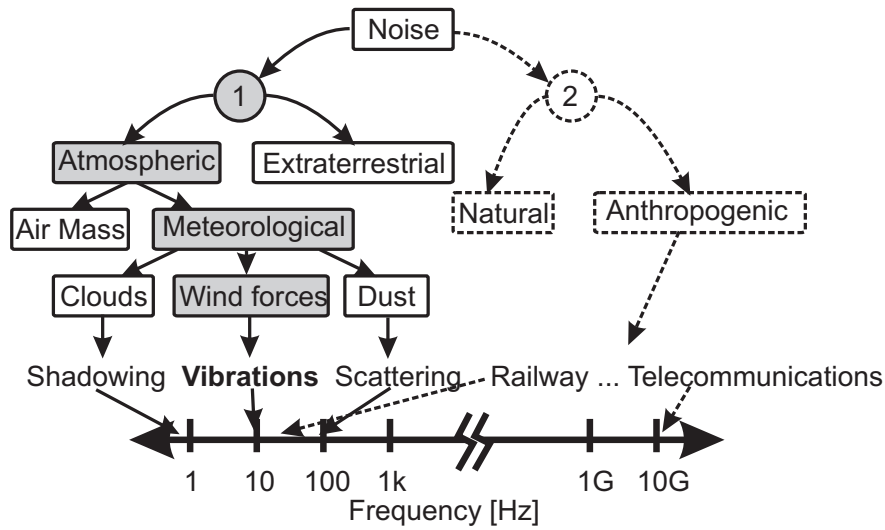
Figure 1.1.
Origin of externally introduced noise in photovoltaic solar cells with examples
and typical frequency ranges: Light fluctuations (1) are branched as
continuous line, radio frequency emissions (2) are represented as dotted lines.

of a mounting construction is in the low to very low frequency range. As previously reported noise amplitudes below 100 Hz sometimes became the major contribution to the observed noise spectra and were attributed to wind induced vibrations[11, 29, 30, 31].

Especially large photovoltaic power stations with more than 1 MW_P are often placed in sparse regions, with high sunlight exposure. This leaves the power plant exposed to wind forces, without there being any natural obstacles, resulting in higher wind speeds near ground level [35].

The effect of wind velocities has been included many times as an important variable in the performance of photovoltaic power plants [21, 22]. However the effect of this variable remains uncertain or is directly linked to the thermal condition of a solar module [13, 18]. While the cooling of wind results in a slightly increased performance of the PV power plant, the entailed vibrational disturbances are often ignored.

This thesis is divided into 6 chapters. In chapter 2 the theoretical concepts, relevant to this work are outlined.

In chapter 3 a solar module was mounted on the roof top of the physics institute in Vienna to conduct a case study, of the effect of wind induced vibration on the performance of a solar module, under ambient conditions. A statistical analysis

was undertaken (section 3.4.1) and the effect of different angles of incident light were investigated (section 3.4).

In chapter 4 a solar module/solar cells were mounted to a vibration table. To support the analysis of chapter 3 section 3.4 the angle dependency of the solar module has been examined in section 4.4. Additionally the effect of the a.c. noise under different load resistances and circuit arrangements was investigated (section 4.3).

In chapter 5 an electronic simulation was carried through. This was done to supplement and confirm the results of chapter 4 section 4.3. The last chapter contains the conclusion of the thesis.

2. Theory

In this chapter the basic working principle of a solar cell will be summarized shortly. An emphasis is laid on optical characteristics and the astronomical background, since these are phenomena closely connected to the subject of research at hand. Additionally the electrical characteristics of solar cells, the circuitry of modules, types of inverters and maximum power point trackers will be discussed. The general information presented in this chapter, unless otherwise referenced, was obtained from: [19, 24, 36].

2.1. Basic principle of solar cells

2.1.1. Solar cell

The solar cell is the fundamental building block of any photovoltaic system. As an electric power generation unit it can be seen as a two terminal device. In the dark it behaves like a diode, blocking in one direction and conducting in the other. When illuminated it generates a photo voltage. When exposed to sunlight a single solar cell generates a d.c. photo voltage of roughly 0.5 V but can go up to 1 V. When operated under short circuit it produces a photo current of some tens of mA/cm^2 [24, p. 4].

The basic principle of solar cells is based on the photoelectric effect. It states that electrons can be emitted from matter, when they absorb a photon. In the case of a simple photovoltaic device the energy of the photon is used to excite an electron from the valence band to the conduction band, thus generating an electron hole pair. The energy range between these two states, where no electron state exists, is called *band gap* or *energy gap*. The electron-hole pair exists only for a very short time, the lifetime τ, before it recombines to the energetically favorable state.

2.1.1.1. Doping and the p-n junction

Doping is the process where impurities are introduced into an otherwise extremely pure semiconductor. This changes the electrical properties of the doped material. In the photovoltaic industry doping is done, to create a *p-type* and an *n-type* semiconductor.

P-type semiconductors derive their name from the positive charge carriers they set free. *N-type* semiconductors set negative charge carriers free and provide extra conduction electrons. When these two are put together very closely, on an atomic level, a *p-n junction* is formed.

In the case of silicon solar cells atoms from group III of the periodic table are used as p-type dopants. This results in one electron missing from one of the four covalent bonds in the crystal matrix of silicon.

N-type dopants on the other hand provide extra conduction electrons to the host material, with a very low binding energy. For silicon cells elements from group V, preferentially phosphorus, are used for this.

In III-V semiconductors two different elements, one from group III and one from group V are joined to form a compound semiconductor. Gallium arsenide (GaAs), where gallium and arsenic are joined, is the most common of these semiconductors. For the n-type doping of gallium arsenide usually silicon is used as dopant, where it takes the place of gallium in the molecular structure of GaAs. For the p-type doping, usually carbon substitutes arsenic [24, p. 201].
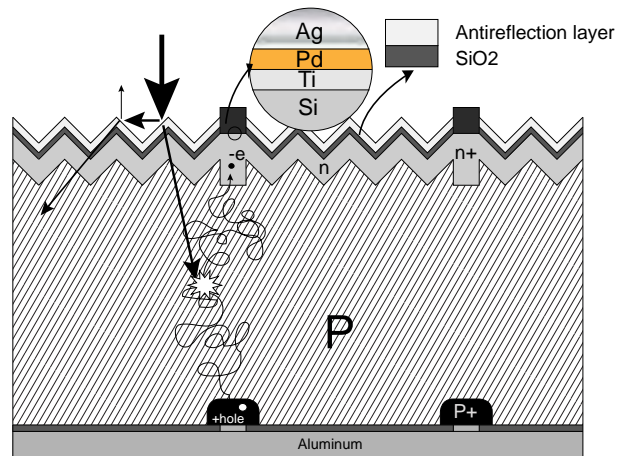
Figure 2.1.
Basic working principle of a silicon based solar cell. The serrated profile of
the surface stems from an anti-reflection structure. (rework from
www.wikipedia.org)

At the boundary, between the n- and p-type region, electrons diffuse from the
n-type to the p-type region and holes from the p-type to the n-type region. This
results in an excess of positively charged ions in the n-type region and negatively
charged ions in the p-type region, thus creating an electric field.

Figure 2.1 shows a photon, which gets absorbed by an atom in the p-type region
of a solar cell (marked as white star). This creates an electron hole pair. The
electron is now able to move freely in the conduction band, it remains there
for a certain time span τ until it recombines to the energetically favorable state
(see section 2.1.2). During this time the electron typically travels a distance L.
The probability for an electron to reach the depletion zone, between n- and p-
type region, during its life time in the conduction band decreases exponentially,
with the distance from the depletion region. If it reaches the depletion region it
accelerates towards the n-type region. Holes are minority carriers in the n-type
region. From there, they get pushed into the p-type region, if they reach the p-n
junction.

At the contacts on the backside of the solar cell a heavily doped p+ region is
shown. This reduces the rear surface recombination and creates another $p - p+$
junction, which acts as a potential barrier for minority electrons in the p-type
region [24, p. 191].

The stream of electrons to the terminals of the n-type region and the stream of
holes to the p-type region, creates a current. Thus the solar cell is modeled as
a current source in parallel with a diode in an equivalent circuit diagram, as is
explained in section 2.5.2.

2.1.2. Types of solar cells

For a photovoltaic device to work efficiently several criteria have to be met. Efficient light absorption, efficient charge separation and efficient charge transport are vital [24, p. 177]. Furthermore:

- The reflectivity of the surface should be small.

- The band gap should be close to the optimum for the intended solar spectrum [24, p. 178].

- Electron-hole recombination in the junction region should be low.

- For a good majority carrier transport the series resistance R_s should be small.

Recombination is the process where a mobile charge carrier from the conduction band recombines to the valence band, releasing energy. There are four types of recombination:

1. Radiative recombination:
   The energy gets released through a photon.

2. Auger recombination:
   The energy is given to a third carrier, usually another electron through scattering. The carrier doesn't move to another energy band, but loses its excess energy to thermal vibrations.

3. Shockley Read Hall recombination
   Impurities in the semiconductor are introducing defects or *trap* states in the band gap by capturing free charge carriers. These facilitate every charge carrier in the conduction band to easily release its energy. The Shockley Read Hall recombination is by far the most important in semiconductors.

4. Surface and grain boundary recombination
   At the surface, or at areas where the lattice structure is not continuous, unsaturated valence electrons remain. These open bonds are called dangling bonds and are responsible for additional trap states at the semiconductor's interface.

The theoretical conversion efficiency of a single-junction solar cell depends on the band gap and the spectrum of the incoming light flux. The most common reference spectrum for terrestrial applications is AM1.5. For an explanation of the reference spectrum see section 2.4.4. All photons with an energy below the band gap, cannot be used to gain photo electricity and are transmitted through the solar cell.

The excess energy of photons beyond the band gap ($\hbar\omega - E_g$, see section 2.2) gets usually transformed into heat. To harvest the excess energy of a photon with

more than twice the band gap energy, one has to avoid the thermalization of the charge carriers. This could be achieved by down conversion of the incident high energy photons into two or more lower energy photons, before they enter the solar cell [34].

For the theoretical conversion efficiencies of at least 30 % in AM1.5 the band gap has to be $1.3 \pm 0.3\,\text{eV}$ [24, p. 34]. The theoretical limit of a solar cell with a single p-n junction, for a given spectrum is determined by the Shockley-Queisser limit. It has a maximum of around 41% at a band gap of 1.1 eV for a 6000 K black body spectrum where the solar cell operates at a temperature of 300 K [33].

Additionally there should be a high quantum efficiency over a wide range of wavelengths. The *quantum efficiency (QE)* is defined as the probability that one incident photon of the energy E will deliver one elementary charge to the external circuit [24, p. 27].

Multijunction photovoltaic cells contain two or more p-n junctions, which allows higher efficiencies. The current record for the highest efficiency (43.5 %, in April 2011 [1]) is held by a multijunction cell. Since the production cost per kW_p of these cells is very high, their market share for terrestrial applications is still minor. However they are important for space applications and in concentrating photovoltaics (see section 2.4.7).

2.1.2.1. Silicon solar cells

Being the base material of the whole electronic industry, silicon could be considered as the most important technological material of the last decades. The EPIA[1] estimates the production capacity for monocrystalline silicon cells in 2010 to have been 30 to 35 GW and the global multicrystalline silicon capacity 27 to 28 GW. Whereas the global production capacity of thin film modules has only reached around 3.5 GW in 2010, which includes amorphous silicon and CdTe cells [2]. This displays the dominance of silicon based solar cells in the PV industry.

We will distinguish *multicrystalline* as material where the crystal grain size is comparable with or larger than the device thickness , and *polycrystalline* or *microcrystalline* as material where the grain size is much smaller. [24, p. 178]

Silicon is a semiconductor with an *indirect band gap*. The map of energies E against wave-vectors $\vec{k}$ is called *band structure*. In silicon the wave-vector $\vec{k_V}$ belonging to the highest energy level E_V in the valence band, differs from $\vec{k_C}$, the wave-vector of the lowest energy level in the conduction band [24, p. 50]. For a photon to excite an electron from the valence to the conduction band, an additional momentum is necessary. This momentum has to be derived from a suitable phonon, to guarantee that both momentum and energy are conserved.

---

[1]EPIA = European Photovoltaic Industry Association

Of course this makes the process, of a charge carrier being excited by a photon, far less likely, resulting in a weak absorption ability. Therefore silicon solar cells have to be thicker in order to absorb the light completely. A mono- or multicrystalline silicon cell wafer is usually about $200\,\mu$m thick. In contrast to thin film solar cells, which usually are only a few μm thick. The bulk of the wafer is slightly p-doped with a concentration of $n_A = (10^{15} - 10^{16})/\text{cm}^3$. Whereas the comparatively heavy n-doped layer is usually only about 1μm thick and facing the sun [36, p. 127]. On the backside of the solar cell there is again a thin layer that's heavily p-doped creating the back surface field, as schematically illustrated in figure 2.1

The most common n-type dopant for silicon is pentavelant phosphorus. For p-type doping most frequently trivalent boron is used.

Since the penetration depth of the depletion region is inversely proportional to the doping concentration, the depletion region stretches further into the lightly p-doped area, than into the n-doped area.

In monocrystalline silicon the crystalline structure is ideally continuous and unbroken throughout the whole wafer. In multicrystalline silicon, the areas of the monocrystalline-like lattice configuration usually cover several mm^2, and are confined by grain boundaries. On the grain boundaries, defects accumulate. But also the rest of the wafer is more prone to defects than in ordinary monocrystalline silicon. Its total conversion efficiency is usually a little below that of monocrystalline silicon, but due to lower production costs it gets employed a lot [19, p. 51].

2.1.2.2. Monocrystalline and thin film solar cells

In monocrystalline solar cells the p-n junction forms due to different dopants being deployed in the p- and in the n-region. They have the advantage that there is no material interface at the junction. The great majority of these cells deployed are silicon solar cells. It is also the only elemental semiconductor with an applicable band gap, to harvest photons coming from the sun efficiently. However there are some disadvantages to using silicon (see section 2.1.2.1). The most common alternative of monocrystalline cells are III-V semiconductor materials, where an alloy, containing equal numbers of atoms from groups III and V, is deployed.

Thin film cells are made by depositing one or more thin layers on a substrate. The deposition happens either chemically or physically and allows fast throughput of large areas [24, p. 211]. The thickness of these layers varies but is always well below the thickness of a bulk silicon cell. There are several architectures for thin film cells, among the most widely produced are:

- Amorphous silicon (a-Si).

- Multicrystalline cadmium telluride (CdTe).

- Multicrystalline copper indium diselenide ($CuInSe_2$).

- Microcrystalline thin film silicon ($Mc-Si$).

Usually microcrystalline and amorphous cells contain a higher density of intrinsic defects, leading to an increase in traps. Hence these cells need to be strong optical absorbers to work efficiently. Some of them have p-i-n structures, instead of a direct p-n junction, to widen the depletion region, where less recombination occurs than in the highly doped layers.

2.2. Solar Resource

2.2.1. Black body model

A black body is an idealized model of a body that absorbs radiation at all photon energies $\hbar\omega$ completely. Hence its absorptivity is always one.

$$a(\hbar\omega) = 1 \tag{2.1}$$

Here $\hbar$ is the reduced Planck constant ($\hbar = h/2\pi$) and ω is the angular frequency. An idealized black body emits a characteristic frequency spectrum that only depends on the body's temperature, called black body spectrum. The spectrum of the sun can be approximated by a black body spectrum of $T = 5760\,\mathrm{K}$.

2.2.1.1. The Bose-Einstein distribution

Since photons have an integer spin number, the Bose-Einstein distribution is applicable. It determines the probability of states with the energy $\hbar\omega$ being occupied with photons. The chemical potential can be ignored by photons coming from the sun [36, p. 13], hence the formula is:

$$f_r(\hbar\omega) = \frac{1}{\exp\left(\hbar\omega/kT\right) - 1} \tag{2.2}$$

f_r describes the distribution of the photons only with respect to their energy. For a more accurate model of the distribution of the photons we have to derive the density of the states $D_\gamma(\hbar\omega)$.

2.2.1.2. Density of states for photons

The uncertainty principle by Heisenberg in regard to momentum and position for one particle in one dimension can be defined as:

2. Theory

$$\Delta x \Delta p_x \geq h \tag{2.3}$$

Where Δx is the uncertainty in space along the x-axis and Δp_x is the uncertainty of momentum.

Hence one state in the momentum space and position space takes up the phase space volume:

$$\Delta x \Delta p_x \Delta y \Delta p_y \Delta z \Delta p_z = h^3 \tag{2.4}$$

For a black body the position of a photon is confined to a volume $V = L_x L_y L_z$. We do not know where the photon is within this volume, hence the uncertainty for the momentum is $\Delta p_x \Delta p_y \Delta p_z = \Delta p^3 = h^3/V$. Photons can be polarized, so every momentum space volume Δp^3 can be taken up by two photons.

We now try to find the density of photons states per energy interval. For photons with no rest mass the following relation is valid:

$$\hbar \omega = c|\overrightarrow{p}| \tag{2.5}$$

Where c is the speed of light in a given optical medium. It is connected to the refraction index n by:

$$c = c_0/n \tag{2.6}$$

Here c_0 is the speed of light in vacuum.

All states, where the photon has an energy $\hbar \omega' < \hbar \omega$, hence $|p'| < |p|$, occupy a place within a 3 dimensional sphere with the radius $|p| = \hbar \omega / c$. There number is:

$$N_\gamma = 2 \cdot \frac{4\pi}{3} \frac{p^3}{h^3/V} = \frac{8\pi}{3V} \frac{(\hbar \omega)^3}{h^3 c^3} \tag{2.7}$$

The number 2 indicates the two polarizations of photons.

The density of states, hence the number of states per volume and energy interval can be derived form equation 2.7:

$$D_\gamma(\hbar \omega) = 1/V \cdot \frac{\mathrm{d}N_\gamma(\hbar \omega)}{\mathrm{d}\hbar \omega} = \frac{(\hbar \omega)^2}{\pi^2 h^3 c^3} \tag{2.8}$$

Using eq. 2.6 we see, that by increasing the refraction index n the density of states increases with the third power.

When photons coming from a medium with a high refraction index, enter a medium with a low refraction index with the same distribution $f_r(\hbar \omega)$ there are not enough free states for all photons. This leads to the well known optical phenomenon of total internal reflection.

12

2.2.1.3. Energy distribution of the photons

In the black body model photons behave isotropically. For the distribution of states in the momentum space the density of states per solid angle Ω is defined as:

$$D_{\gamma,\Omega}(\hbar\omega) = D_\gamma(\hbar\omega)/4\pi \tag{2.9}$$

With the density of states (eq. 2.8) and the distribution (eq. 2.2) we now derive a form of *Planck's law*, which determines the number of photons per volume in the solid angle $\mathrm{d}\Omega$ and the energy interval between $\hbar\omega$ and $\hbar\omega + \mathrm{d}\hbar\omega$.

$$\mathrm{d}n_\gamma(\hbar\omega) = D_{\gamma,\Omega}(\hbar\omega)f_r(\hbar\omega)\mathrm{d}\hbar\omega\mathrm{d}\Omega = \frac{(\hbar\omega)^2 \mathrm{d}\Omega}{4\pi^3\hbar^3 (c_0/n)^3} \frac{\mathrm{d}\hbar\omega}{\exp(\hbar\omega/kT) - 1} \tag{2.10}$$

By differentiating the photon density per photon energy interval $\mathrm{d}n_\gamma/\mathrm{d}\hbar\omega$ we derive its maximum at $\hbar\omega = 1.59\,kT$. To get the energy density per photon energy interval $\mathrm{d}e_\gamma/\mathrm{d}\hbar\omega$ one can use the energy per photon $\hbar\omega$, to obtain the energy density, hence:

$$e_\gamma = n_\gamma \cdot \hbar\omega \tag{2.11}$$

$\mathrm{d}e_\gamma/\mathrm{d}\hbar\omega$ peaks at:

$$\hbar\omega_{max} = 2.82\,kT \tag{2.12}$$

To obtain the energy density or the overall radiation energy per volume we use equation 2.11:

$$e_\gamma = \int_0^\infty \frac{(\hbar\omega)^3}{4\pi^3\hbar^3 (c_0/n)^3} \frac{\mathrm{d}\hbar\omega}{\exp(\hbar\omega/kT) - 1} \int_0^{4\pi} \mathrm{d}\Omega \tag{2.13}$$

We substitute with $x = \hbar\omega/kT$ and derive:

$$e_\gamma = \frac{\pi^2 k^4}{15\hbar^3 (c_0/n)^3} T^4 \tag{2.14}$$

To calculate the photon density we can integrate over equation 2.10 and get:

$$n_\gamma = \frac{2.40411 k^3}{\pi^2\hbar^3 (c_0/n)^3} T^3 \tag{2.15}$$

The mean energy of the photons is:

$$\langle \hbar\omega \rangle = e_\gamma / n_\gamma = 2.791 \, kT \tag{2.16}$$

2.3. Optical characteristics

For the consideration of the effect of displacement on the solar cell, the energy flux density has been assumed to be constant for most cases. For image forming systems the conservation is not self evident. Further the effects of refraction and the maximum concentration of sunlight are discussed, as well as the absorption rate.

2.3.1. Kirchhoff's law of thermal radiation

Kirchhoff's law of thermal radiation with respect to the photon energy states that the emissivity $\varepsilon(\hbar\omega)$ equals the absorptivity $a(\hbar\omega)$. The energy flux density j_E emitted from a body in the energy interval $\mathrm{d}\hbar\omega$ and the solid angle $\mathrm{d}\Omega$ is defined as [36, p. 26]:

$$\frac{\mathrm{d}j_E(\hbar\omega)}{\mathrm{d}\hbar\omega} = \frac{a(\hbar\omega)\mathrm{d}\Omega}{4\pi^3\hbar^3(c_0/n)^2} \cdot \frac{(\hbar\omega)^3}{\exp\left(\hbar\omega/kT\right) - 1} \tag{2.17}$$

The energy is based on the emitted photon flux density:

$$\frac{\mathrm{d}j_\gamma(\hbar\omega)}{\mathrm{d}\hbar\omega} = \frac{a(\hbar\omega)\mathrm{d}\Omega}{4\pi^3\hbar^3(c_0/n)^2} \cdot \frac{(\hbar\omega)^2}{\exp\left(\hbar\omega/kT\right) - 1} \tag{2.18}$$

The absorptivity $a(\hbar\omega)$ is a specific property of a body, including its geometry. It is connected to the absorption coefficient $\alpha(\hbar\omega)$, which is a material property. Ignoring multiple reflection we can calculate the transmissivity t of a plate with the thickness d using:

$$t(\hbar\omega) = (1 - r(\hbar\omega)) \cdot \exp\left(-\alpha(\hbar\omega)d\right) \tag{2.19}$$

Using

$$a(\hbar\omega) + t(\hbar\omega) + r(\hbar\omega) = 1 \tag{2.20}$$

with $r(\hbar\omega)$ as the reflectivity, we obtain for the absorptivity of a plate.

$$a(\hbar\omega) = (1 - r(\hbar\omega)) \cdot (1 - \exp\left(-\alpha(\hbar\omega)d\right)) \tag{2.21}$$
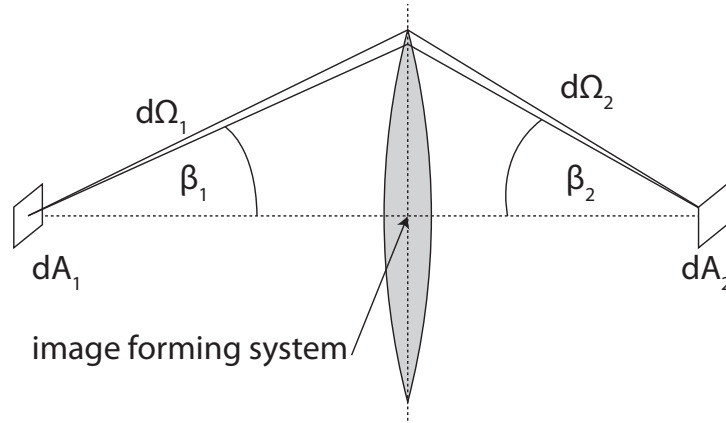
Figure 2.2.
Energy flux density when passing an image forming system.

2.3.2. Conservation of the energy flux

As seen from the earth, the sun has an angle diameter of about $\alpha_s = 32'$ [24, p.19].

This corresponds to a solid angle of:

$$\Omega_s = 2\pi \int\limits_{0}^{\alpha_s/2} \sin\vartheta \mathrm{d}\vartheta = 2\pi \left(1 - \cos\frac{\alpha_s}{2}\right) \tag{2.22}$$

$$\Omega_s = 6.8 \cdot 10^{-5}\,\mathrm{sr}$$

The energy flux density on the earth's surface is about $1\,\mathrm{kW/m^2}$. To gain a higher energy flux density, one has to focus the incoming light with mirrors and optical lenses.

We can use the Helmholtz-Clausius theorem to determine what happens with the energy flux density, when it passes through an image forming system. The two area elements $\mathrm{d}A_1$ and $\mathrm{d}A_2$ depicted in figure 2.2 can both be assumed to be black bodies. Furthermore emissivity and absorptivity, as well as the reflectivity are both non existent for the image forming system in this thought experiment, hence the transmissivity is 1 .

Kirchhoff's law of thermal radiation states that at thermal equilibrium the emissivity of a body equals its absorptivity.

So for the case of equilibrium of temperature, emissivity and absorptivity between the two area elements, is equal. Since this is not only true for every photon energy interval, but also for every interval of direction, this also extends to the solid angle element.

Hence we can conclude:

When passing through an image forming system, that doesn't absorb or emit, the energy flux density per solid angle remains constant [36, p. 32].

The reversibility of the optical path implicates thermodynamic reversibility. This further means that entropy remains constant ($\mathrm{d}S=0$).

2.3.3. The Abbe sine condition

In figure 2.2, the energy flux emitted from $\mathrm{d}A_1$ in the solid angle element $\mathrm{d}\Omega = \sin\beta_1\mathrm{d}\beta_1\mathrm{d}\phi_1$ in the direction (β_1,ϕ_1) is:

$$\mathrm{d}I_{E,1} = j_{E,\Omega,1}\mathrm{d}A_1\cos\beta_1\sin\beta_1\mathrm{d}\beta_1\mathrm{d}\phi_1 \tag{2.23}$$

Here ϕ is the angle around the optical axis, in the plane of the lens, in figure 2.2. Due to the temperature equilibrium this energy flux is identical to the one radiated from $\mathrm{d}A_2$ in the direction (β_2,ϕ_2) in the solid angle element $\mathrm{d}\Omega_2 = \sin\beta_2\mathrm{d}\beta_2\mathrm{d}\phi_2$:

$$\mathrm{d}I_{E,1} = \mathrm{d}I_{E,2} = j_{E,\Omega,2}\mathrm{d}A_2\cos\beta_2\sin\beta_2\mathrm{d}\beta_2\mathrm{d}\phi_2 \tag{2.24}$$

Using equation 2.17 we find that:

$$\frac{j_{E,\Omega,1}}{j_{E,\Omega,2}} = \frac{c_2^2}{c_1^2} = \frac{n_1^2}{n_2^2} \tag{2.25}$$

In order to obtain the complete energy, emitted or absorbed by $\mathrm{d}A_2$, we have to integrate over the whole lens. We define ν_2 as the angle where β_2 points to the tip of the lens. We integrate ϕ from 0 to 2π:

$$I_{E,2} = j_{e,\Omega,2}\mathrm{d}A_2\pi\sin^2\nu_2 \tag{2.26}$$

Analogously:

$$I_{E,1} = j_{e,\Omega,1}\mathrm{d}A_1\pi\sin^2\nu_1 \tag{2.27}$$

Since under temperature equilibrium the above equations are equal we can state the Abbe sine condition:
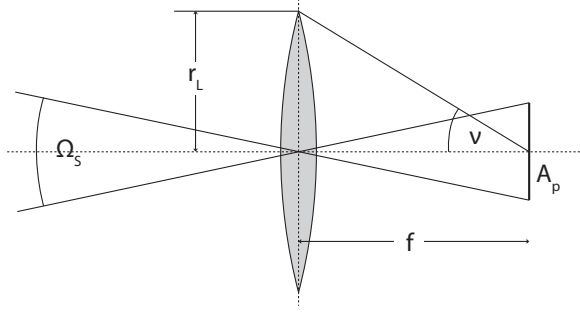
Figure 2.3.
Image of the sun with the area A_p in the focal plane of a lens with the radius
r_L and the focal distance f.

$$n_1^2 \mathrm{d}A_1 \sin^2 \nu_1 = n_2^2 \mathrm{d}A_2 \sin^2 \nu_2 \tag{2.28}$$

The Abbe sine condition, as given by eq. 2.28 is founded on the conservation of energy flux density per solid angle, for areas with the same refraction index, when they pass through an image forming system. It is by no means trivial, since it contradicts the laws of geometrical optics.

2.3.4. Concentrated sunlight

In figure 2.3 we see a schematic depiction of a lens bundling sunlight. The energy flux falling on the lens, assuming a refraction index $n = 1$, is:

$$I_E = j_{E,sun} \pi r_L^2 \tag{2.29}$$

Where $j_{i,sun}$ is the energy flux density of the sunlight at the lens. For the image A_p the energy density is:

$$j_{E,image} = I_E/A_P = j_{E,sun} \pi r_L^2 / A_p \tag{2.30}$$

The concentration C is according to geometrical optics:

$$C = \frac{j_{E,image}}{j_{E,sun}} = \frac{\pi r_L^2}{A_p} \tag{2.31}$$

If we want to determine the maximum concentration it does not suffice to merely use geometrical optics. By doing so we would be able to increase the concentration

indefinitely. So we have to consider the conservation of the energy flux density per solid angle of the sun. Using equation 2.26 we obtain:

$$j_{E,image} = j_{E,sun}\pi \sin^2 \nu \tag{2.32}$$

After passing through the lens, the sunlight fills a cone with the aperture angle ν. Using equation 2.31 we obtain:

$$C = \frac{\pi}{\Omega_s} \sin^2 \nu \tag{2.33}$$

The theoretical maximum for this concentration is reached for $\nu = \pi/2$. The theoretical maximum concentration of sunlight through an image forming system thus is 46200. This is only valid for an refraction index $n = 1$ for the adjoining optical medium. For sapphire, for which $n = 1.76$ a record concentration of 84000 has been reached experimentally [19, p. 237].

2.3.5. Generation of electron-hole pairs and optical implications

Using the equations from section 2.3.1 the overall absorbed photon flux density $j_{\gamma,abs}$ is a fraction of the incoming photon flux density $j_{\gamma,inc}$ [36, p. 76]:

$$j_{\gamma,abs} = (1 - r - t)j_{\gamma,inc} = (1 - r)\left(1 - \exp(-\alpha d)\right)j_{\gamma,inc} = a \cdot j_{\gamma,inc} \tag{2.34}$$

Again here we ignore the case of multiple reflections. Since for every absorbed photon an electron and a hole is generated, their rate of generation is:

$$G_h = G_e = \alpha j_\gamma(x) \tag{2.35}$$

Where x is the distance in the direction of the incoming light beam, G_h is the generation rate of holes and G_e that of electrons.

We now look at the rate of absorption of photons under a dark $T_0 = 300\,\mathrm{K}$ ambient and denominate these equilibrium rates with a super scripted zero. Using equations 2.34, 2.35 and 2.18 we derive:

$$G_h^0 = G_e^0 = \int\limits_0^\infty \alpha(\hbar\omega)\mathrm{d}j_\gamma(\hbar\omega) \tag{2.36}$$

$$G_h^0 = G_e^0 = \frac{\Omega}{4\pi^3\hbar^3(c_0/n)^2} \cdot \int\limits_0^\infty \alpha(\hbar\omega)\frac{(\hbar\omega)^2}{\exp\left(\hbar\omega/kT_0\right) - 1}\mathrm{d}\hbar\omega \tag{2.37}$$
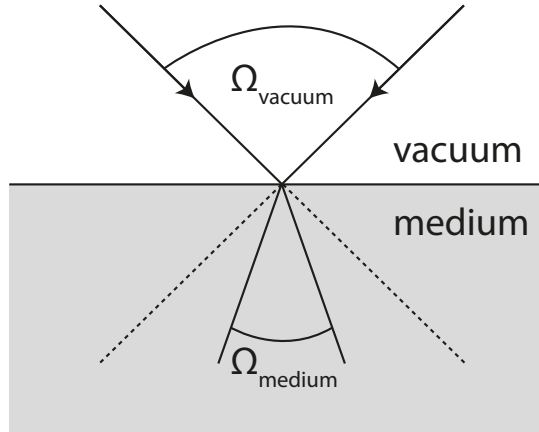
Figure 2.4.
Photons passing from vacuum to a medium. In the medium the solid angle
they fill up is smaller than in the vacuum.

The photon flux density per solid angle and therefore the absorption rate of photons is directly proportional to n^2. Since the photon flux density isn't changed, apart from reflection, the photon flux density per solid angle has to be reduced by the factor n^2. This means that certain parts of the solid angle in the medium cannot be reached, as illustrated by figure 2.4 This is also covered by Snell's law and the effect of total internal reflection.

2.4. Astronomical background

2.4.1. The earth centered celestial sphere

To calculate the position of the sun on the sky it is helpful to introduce the *earth centered celestial sphere.* It is imaginary, has an infinite large radius and is concentric with the earth and rotating on the same axis. Hence the earth centered celestial sphere is a geocentric inertial frame of reference. It is shown in figure 2.5, where the yearly revolution of the sun around the earth is represented. It is tilted 23.44 deg or 0.409 rad, since the rotational axis of the earth with regard to its revolution around the sun is also tilted. The *solar declination δ* is the angle between the line joining the centers of the sun the earth and the equatorial plane. It can be assumed to be constant, during the course of a day [19, p. 11]:
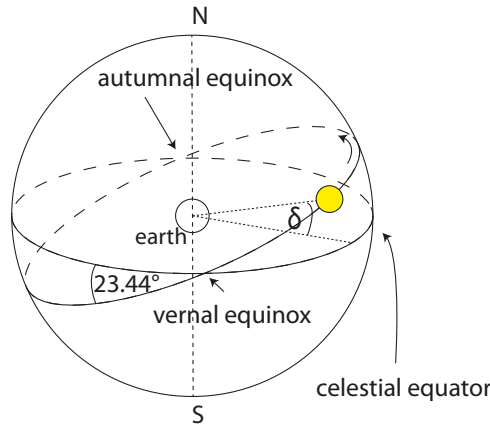
Figure 2.5.
The earth centered celestial sphere and the yearly motion of the sun in its
frame of reference.

$$\delta = \pi \frac{23.44}{180} \sin\left(2\pi \frac{284 + n}{365}\right) \tag{2.38}$$

The angle here is given in radian, where n denominates the nth day of the year, starting with January 1st. On the summer solstice of the northern hemisphere δ reaches the maximum of $0.409\,\text{rad}$. The celestial sphere can also be centered with an observer.

2.4.2. Angle definitions from the point of an observer

From the point of an observer standing on the surface of the earth, a different set of angles is used to describe the current position of the sun. It is shown in figure 2.6. When drawing a straight line from the center of the earth, through the observer, it points to the *zenith*. The angle between the zenith and the current position of the sun, from the point of an observer is called *zenith angle* θ_Z . The *solar elevation* α is the angle between the line joining the observer, the sun and the idealized horizon (the plane going through the observer, perpendicular to the line from the center of the earth to the observer). Hence:

$$\theta_Z + \alpha = \pi/2 \tag{2.39}$$

The *solar azimuth* τ is zero at solar high noon and increases towards the east.
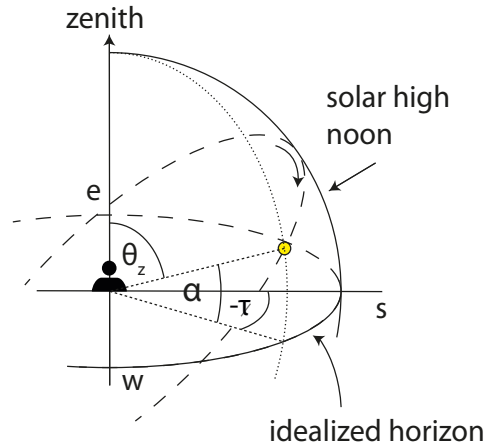
Figure 2.6.
Here the apparent daily motion of the sun, from the point of an observer, on the surface on the earth on the northern hemisphere is shown. τ is the azimuth, α the solar elevation and θ_z the zenith angle. Additionally the cardinal directions east, west and south are depicted.

2.4.3. Transformation equations

In this chapter the formulas to express the solar elevation α and the solar azimuth τ explicitly, from angles in the frame of reference of the earth centered celestial sphere, are given. The solar azimuth τ is defined here with the south as reference where $\tau = 0$ and has a negative sign, when turning west as can be seen in figure 2.6.

We denominate the *geographical latitude* as ψ. The *hour angle* ω is defined in the frame of reference of the earth centered celestial sphere, but depends on the position of the observer, on the earth. It is the angle between two planes. One is the plane containing the earth's axis and the zenith of a given observer and the other one is the plane between the earth's axis and the sun.

The solar elevation for an observer on the latitude ψ, with a solar declination δ (defined by the day of the year) and an hour angle ω (dependent on the time of day, and the longitude of the observer's location), can now be calculated:

$$\sin \alpha = \cos \theta_Z = \sin \delta \sin \psi + \cos \delta \cos \psi \cos \omega \qquad (2.40)$$

The solar azimuth:

$$\cos \tau = (\sin \alpha \sin \psi - \sin \delta) / \cos \alpha \cos \psi \qquad (2.41)$$
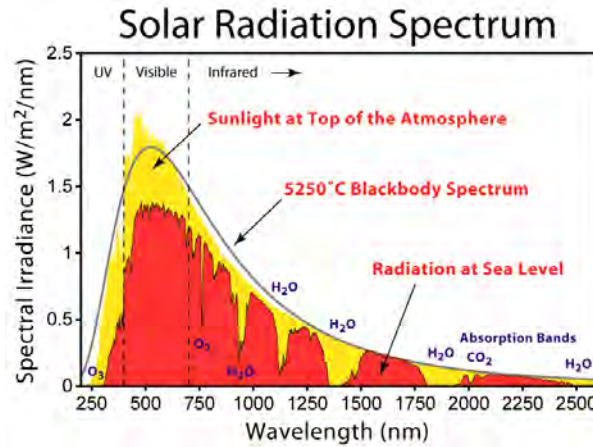
Figure 2.7.
The solar irradiance spectrum above the atmosphere is shown in yellow and on the surface at sea level it is shown in red. The black line shows the idealized black body spectrum for a body with a temperature of roughly 5523 K. (From www.wikipedia.org)

These equations can be used to calculate the *sunrise hour angle* ω_S.

$$\omega_S = \cos^{-1}\left(-\tan\psi\tan\delta\right) \tag{2.42}$$

This is the angle between the meridian of solar high noon and the meridian where the sun will rise, for an observer standing at the latitude ψ during a day where the solar elevation is δ.

2.4.4. Definition of the air mass index

When passing the atmosphere, the radiation of the sun gets partly absorbed and scattered. Wavelengths below 300 nm are filtered out by oxygen, ozone and nitrogen. The various dips in the spectrum stem from gases with low concentration like H_2O, CO_2, N_2O and CH_4. The dips for H_2O and O_2 are illustrated in figure 2.7.

Attenuation by the atmosphere is quantified by the Air Mass factor $n_{AirMass}$ which is defined, for $\alpha > 0$, by:

$$n_{AirMass} = 1/\sin\left(\alpha\right) \tag{2.43}$$

The spectrum outside the atmosphere is denominated as AM0. The typical spectrum for temperate regions is AM1.5 where $n_{AirMass} = 1.5$. This is defined as

the standard spectrum to compare the efficiency of terrestrial solar cells (section 2.5.3). The integral over this spectrum, the energy flux density on a surface mounted perpendicular to the sun on a cloud free sky, is set to:

$$j_{E,AM1.5} = 1.0\,\text{kW/m}^2 \qquad (2.44)$$

2.4.5. Radiation on an inclined object

Although the air mass index is widely used it is not a very precise assessment of the incoming energy flux. The *solar radiation* for a specific site (if available) is usually given in the form of global radiation on a horizontal surface at a specific site and denoted as G. It is measured in J/m^2 and describes the integral of the energy received over 24 hours. To calculate the daily radiation on an inclined object several steps are required.

First one has to separate *diffuse* and *direct* contributions of sunlight. To accomplish this, the extraterrestrial irradiation B_0 is used as reference. It is measured in J/m^2 and describes the irradiation received for a particular day of the year for a unit horizontal area outside the earth's atmosphere, for a given latitude ψ, integrated over 24 hours. The formula to calculate B_0 is [23, p. 37]:

$$B_0 = \frac{3600 \cdot 24}{\pi} \cdot S\left(1 + 0.033\cos(2\pi n/365)\right)\left(\cos\psi\cos\delta\sin\omega_S + \omega_S\sin\psi\sin\delta\right) \qquad (2.45)$$

$3600 \cdot 24$ is the number of seconds during a day. ω_S must be given in radian. S is the solar constant and n is the nth day of the year starting on the 1st of January. The solar constant S is defined as $S = 1367\,\text{W/m}^2$ [19, p. 7]. It is a fixed value by definition, based on the solar radiation in free space at a distance of one astronomical unit from the sun. The first term in brackets considers the eccentricity of the earths orbit, which causes intensity oscillations of approximately $\pm 3,3$ % per year.

K_T describes the average attenuation of solar radiation by the atmosphere, at a specific location during a year. It is connected with B_0 and G through the formula:

$$K_T = G/B_0 \qquad (2.46)$$

To calculate the fraction of diffuse sunlight D/G there are various empirical formulas available. The formula used by [25] is simple and quite accurate for temperate regions:

$$D/G = 1 - 1.13 \cdot K_T \qquad (2.47)$$

2. Theory

The fraction of diffuse sunlight is very important because, direct sunlight is the crucial factor for vibration induced distortions [28]. For further explanations see section 4.4.

The direct radiation hence is defined as:

$$B = G - D \qquad (2.48)$$

The direct radiation $B(\kappa)$ on a south-facing panel in the northern hemisphere inclined at an angle κ to the horizontal surface is given by [19, p. 16]:

$$B(\kappa) = B\frac{\cos(\psi - \kappa)\cos\delta\sin\omega_0 + \omega_0\sin(\psi - \kappa)\sin\delta}{\cos\psi\cos\delta\sin\omega_s + \omega_s\sin\psi\sin\delta} \qquad (2.49)$$

$\omega_0 = \min\{\omega_s, \omega_s'\}$. ω_s has been defined in equation 2.42 and ω_s' is the angle above a plane inclined at angle κ to the horizontal:

$$\omega_s' = \cos^{-1}\left(-\tan(\psi - \kappa)\tan\delta\right) \qquad (2.50)$$

The diffuse radiation on the inclined surface, for the case of isotropic distribution is:

$$D(\kappa) = \frac{1}{2}(1 + \cos\kappa)D \qquad (2.51)$$

The third relevant source of radiation is the albedo from the ground R. It is highly dependent on the surface and the topographic characteristics of the surroundings. For example mountains, or any surface irregularities in the vicinity of the photovoltaic system, can greatly increase the fraction of light reflected towards it. For dry ground the reflectivity is around 0.2, for desert sand about 0.4 and for snow it can go up to 0.8. [19, p. 17]. The albedo radiation can become important for bi facial modules, where front an rear of the panel can harvest energy. However R is rarely measured directly and usually included in the fraction of the diffuse radiation:

$$R(\kappa) \propto (1 - \cos\kappa) \qquad (2.52)$$

The total global irradiation $G(\kappa)$ on the inclined surface hence is:

$$G(\kappa) = B(\kappa) + D(\kappa) + R(\kappa) \qquad (2.53)$$

This model only considers the effect of shadows caused by the typical cloud coverage of a specific site, averaged over one year, insofar as it affects the proportion of the direct radiation B to the diffuse radiation D. Effects caused by shading of the immediate surrounding area, like trees, are ignored.

24

2.4.6. Sunlight tracking and mounting constructions

In most arrays, the modules are mounted at a fixed inclination facing directly towards the equator. This arrangement minimizes the misorientation towards the sun and thus maximizes the dose of sunlight radiation received during the course of a year. This solution, which doesn't require a lot of maintenance, is rivaled by tracking systems. In a two axis tracker, where the panel is always directed ideally towards the sun, up to 40% more of the solar energy can be collected over the years, compared to a fixed tilted installation. However the increased yield, due to tracking, is highly dependent on the installation site and two axis trackers require a lot of maintenance. The advantages gained by them depend on the latitude and the fraction of the direct sunlight contribution B over the year. Since the optimum angle towards the sun depends mainly on the latitude, single axis trackers can be a good compromise. Further it has been estimated that in sunny climates a flat array given a tilt adjustment manually twice a day, can intercept nearly 95% of the energy collected with a fully automatic two-axis tracking [19, p. 92].

2.4.7. Concentrating photovoltaics

In CPV (concentrating photovoltaics) lenses and mirrors are used to focus sunlight on a photovoltaic cell, with the area covered by the focusing system being substantially larger than the one covered by the photovoltaic cell. These systems range from simple designs with side booster mirrors, to concentration systems which employ sophisticated optical techniques to increase the light input by several orders of magnitude.

When deploying CPV, the efficiency gain from each photovoltaic cell has to be weighed against the cost of the concentrating optical system. However this different cost analysis allows the use of sophisticated, higher-efficiency types of cells, which normally wouldn't be competitively viable. One major disadvantage is the increased temperature, that comes with CPV, which diminishes the efficiency of the solar cell.

Once the concentration ratio exceeds 10, tracking becomes indispensable [19, p. 92].

Due to the higher energy flux density, high-efficiency types of solar cells like GaAs, become economically viable. However only direct sunlight can be concentrated, therefore diffuse sunlight (see eq. 2.47) of the AM1.5 spectrum cannot be yielded [24, p. 263].
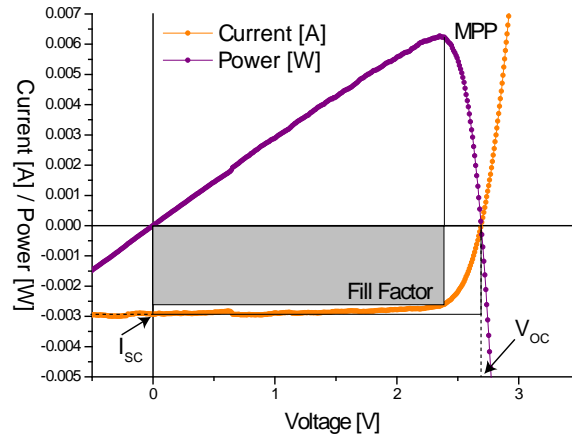
2. Theory

Figure 2.8.
Power and current as a function of voltage of an a-Si miniature module. For
the orange $I(V)$ curve the current has been plotted negatively, to show the
resemblance to the current voltage characteristic of a diode. For the blue line,
showing the resulting power, the sign has been changed to illustrate the
power output of the device.

2.5. Electrical characteristics

2.5.1. Characteristic curve

The characteristic voltage-current curve of a solar cell gives quite extensive infor-
mation about the electrical properties of a solar cell. It is usually obtained by
providing a known voltage and measuring the resulting current or vice versa as
will be discussed in section 4.3.1. The characteristic curve can also be obtained,
by just varying the load resistance in small steps, while recording current and
voltage. The characteristic curve of a solar module recorded in the laboratory in
Vienna is shown in figure 2.8.

Some key parameters are marked in figure 2.8. In an electrical circuit a solar cell
can take the place of a battery, as source of electrical energy, which of course
only works when illuminated. The related load resistor is R_L, as sink of electrical
energy. The case where the two terminals are disconnected ($R_L \to \infty$, $I = 0$)
is called *open circuit voltage* V_{oc}. The current drawn when the terminals are
short circuited ($R_L = 0$, $V = 0$) is called *short circuit current* I_{sc}. For any load
resistance in between ($0 < R_L < \infty$), the cell develops a voltage according to
$V = IR_L$. $I(V)$ is called the *current-voltage characteristic* or *characteristic curve*
of the cell. For each level of illumination the characteristic curve shifts along the
current axis. I and V are both determined by the illumination as well as the load.
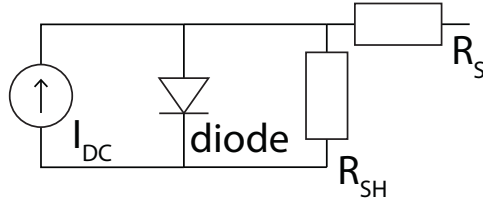
Figure 2.9.
Equivalent circuit diagram of a solar cell modeled as current generator.

It can be seen, that the power output $P = I \cdot V$ reaches a maximum P_{max} at a certain point called the *maximum power point (MPP)*. Obviously one wants to operate the solar cell as close to the maximum power point as possible, this is done by properly adjusting R_L (see section 2.6.3.3). Additionally the *fill factor* is illustrated. It is defined as the ratio of the maximum obtainable electrical power, to the product of the open circuit voltage and short circuit current. In figure 2.8, it is the ratio of the area of the gray rectangle, to the area of the larger rectangle with one corner point at V_{oc} and I_{sc}.

$$FF = \frac{P_{max}}{V_{oc} \cdot I_{sc}} \leq 1 \tag{2.54}$$

Cells with a high fill factor have a low equivalent series resistance and a high equivalent shunt resistance. So the internal losses of the solar cell are decreasing with a high fill factor. Commercial cells usually have a fill factor > 0.7 [24, p. 12].

A solar cell can be modeled as a *current generator*, since there is quite a large spectrum of resistance values for which the current drawn remains almost constant, as can be seen in figure 2.8.

2.5.2. Equivalent circuit model

In order to simulate the behavior of a solar cell and to conduct an analytical analysis, one has to be able to describe the solar cell, by defining its key elements. This can be done by an *equivalent circuit diagram*, like it is shown in figure 2.9.

In solar cells leakage currents around the side of the device occur and power is dissipated through the resistance of the contacts. These losses are equivalent to two resistors, one in parallel R_{sh} (shunt resistance) and one in series R_s. Under concentrated light the current densities increase, and the whole characteristic curve is shifted along the current axis. This increases the voltage drop, caused by the series resistance. The central component of this diagram is, apart from the current source, the diode. For the case of no illumination, where $I_{DC} = 0$, a very

high shunt resistance $R_{sh} \to \infty$ and no series resistance R_s the solar cell behaves like an ideal diode. This is not surprising considering the basic design of a solar cell is analog to a semiconductor diode with a p-n junction.

For an ideal diode the current as a function of voltage and temperature is defined as [24, p. 14]:

$$I = I_O \left(\exp \left(\frac{qV}{kT} \right) - 1 \right) \tag{2.55}$$

Where I_O is the reverse saturation current and q is the magnitude of the elementary charge. The whole circuit as modeled in figure 2.9 is described by the following formula:

$$I = I_{sc} - I_O \left(\exp \left(\frac{q(V + IR_s)}{NkT} \right) - 1 \right) - \frac{V + R_s I}{R_{sh}} \tag{2.56}$$

R_s is the parasitic series resistance and the R_{sh} is the shunt resistance which accounts for the leakage currents. N is a dimensionless factor, heeding that the diode current does not necessarily arise only from diffusion, as assumed in eq. 2.55.

2.5.3. Standard operation conditions

Irradiance	1 kW/m^2
Spectral distribution	AM1.5
Cell temperature	25° C

Table 2.1.
Standard operating conditions for a solar cell.

For the comparison of different solar cell models, it is helpful to define *standard operation conditions* or *standard test conditions*.

The air mass index was explained in section 2.4.4. The temperature coefficient for the open circuit voltage V_{oc} of a single silicon cell is negative and approximately $-2.3 \frac{\text{mV}}{\text{°C}}$. The current coefficient is very small and positive, approximately $+6 \frac{\mu\text{A}}{\text{°C}}$ for a square centimeter of a silicon cell [19, p. 87]. These are approximate, empirically derived values.

2.6. The photovoltaic generator

2.6.1. Structure of a photovoltaic system

The two main categories of photovoltaic systems are *grid-connected* and *stand-alone*. The simplest form of the latter is a photovoltaic generator connected

to a load, which is driven whenever there is sufficient illumination. A typical application for this is a pumping systems, where no constant availability of power is required. When power is required independently from the sun's position a battery for storage is needed in addition.

Grid connected Systems can be divided into *grid back-up systems* which act as an auxiliary supply and *grid interactive systems* which receive excess power from the PV generator. In *PV power stations* the generated power is wholly transmitted to the grid. The main focus of this work is directed at these applications.

Generally speaking a photovoltaic system consists of the following parts.

- The photovoltaic generator with mechanical support and eventually a sun tracking system.

- Batteries which act as storage subsystem (especially in stand alone systems).

- Power conditioning and control equipment (e.g. maximum power point tracker and DC/DC or DC/AC converters).

- Optionally a back-up generator.

2.6.2. The photovoltaic module

Several solar cells connected together and sealed for protection against ambient conditions in one casing are referred to as a *module*. Several modules mounted on one construction are called a *panel* and several panels connected together are called an *array* of solar cells.

Most often the cells in a module are interconnected in series. A $10\,\mathrm{cm} \times 10\,\mathrm{cm}$ multicrystalline solar cell will provide between 1 and 1.5 W power under standard conditions (see table 2.1). Since the voltage of a single solar cell is directly dependent on the energy gap between the valence band and the conduction band of the semiconductor it usually delivers about 0.5 to 0.6 V when sufficiently illuminated. Most appliances don't work at this low voltage. The immediate solution is to connect the solar cells in series. Therefore the number of cells connected in series in a module is governed by the voltage. Many modules have 36 solar cells connected in series which is practical to charge a 12 V battery under less than perfect conditions, and ensures quite reliable operation.

2.6.2.1. Interconnection of photovoltaic modules or cells

The Interconnection of the PV modules and the solar cells is a very critical variable in any analysis of voltage disturbances. The propagation, intensification or resonance effect of any power fluctuation is strongly dependent on the circuit arrangement of the solar cells and modules.
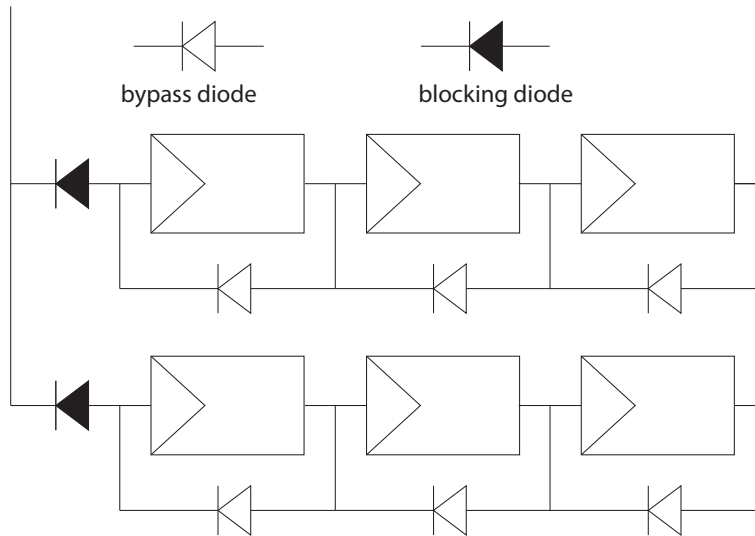
Figure 2.10.
Blocking and bypass diodes in a photovoltaic generator.

In figure 2.10 we see an example of several modules connected. The number of modules connected in series determines the voltage, while the number of modules connected in parallel determines the current provided by the PV generator.

If a solar cell is not illuminated the short circuit current I_{sc} is zero. Eq. 2.56 describes a mere diode which is connected to an external circuit. In case an external voltage source is applied in forward direction, a current flows through the solar cell. This can damage the solar cell and it will drain the voltage source. The obvious solution is to separate the PV generator and the voltage source by a *blocking diode* like shown in figure 2.10. When the battery voltage exceeds the voltage of the module the diode prevents the battery from discharging. Additionally if a single module is obscured it behaves like a diode in reverse direction, blocking the power output of the other cells. Therefore each module has a bypass diode connected in parallel to the module.

To find the best interconnection for a PV-system is still a subject of research. Basically the nominal operating voltage of the system has to be matched to the nominal voltage required by the subsequent load. Naturally the electrical output power of the system is the function to maximize. However, many constraints have to be taken into account. Namely the current-voltage characteristic of the PV module and the energy balance at the level of the module. The ambient temperature has an important impact on the performance and $I(V)$ curve of the system. Furthermore, the diode characteristic of solar cells, which favors, among other factors, the propagation and amplification of distortion signals, has to be taken into account. A more detailed view on the interconnection of solar cells is

given by [6].

2.6.3. Converter technology

In most applications switching power converters are used to transform d.c. power. These converters are widely used in photovoltaic generating systems as an interface between the module, panel or array and the load. Their design allows them to adjust their input voltage without changing the output voltage and therefore makes them perfect for tracking the maximum power point (MPP). [5, 17, 19, 26] An analysis of the impact of the superimposed distortion, caused by vibrations, on converters is given in [32].

2.6.3.1. DC/DC converters

Figure 2.11 illustrates the basic circuit topology of a buck and boost converter. V_i is the voltage at the input, whereas V_o is the voltage at the output. The buck converter reduces the ratio V_i/V_o while the boost converter increases it. V_i/V_o is controlled by the switching frequency and the duty cycle δ_c. The switch S is electronic, usually a *field effect transistor* (MOSFET) or for higher power application an *insulated gate bipolar transistor* (IGBT). The duty cycle δ_c is defined as the ratio between the time the switch is on T_{on} and the commutation period T_C. Hence $\delta_c = T_{on}/T_C$. Usually the switches are driven at a constant frequency. In order to change the load for V_i the duty cycle δ_c is varied. This is called *pulse width modulation* (PWM). It is also possible to vary the frequency in order to change the duty cycle δ_c. This is referred to as *pulse frequency modulation* (PFM).

There are two operational modes: *Continuous conduction operational mode* (CCM) and *discontinued conduction operational mode* (DCM). In the latter one the current that circulates through the inductance of that converter is completely canceled out for a period of time of the commutation period T_C, while in the CCM it's never canceled out completely. In CCM the ratio of load voltage, V_o to the output voltage V_i is only defined by the duty ratio. For a buck converter it is given as:

$$\frac{V_o}{V_i} = \frac{1}{1 - \delta_c} \tag{2.57}$$

While for a boost converter it is:

$$\frac{V_o}{V_i} = \delta_c \tag{2.58}$$

However in both modes these basic converter topologies can be compared to a continuous current transformer. A more detailed description is given in [19, p. 98].
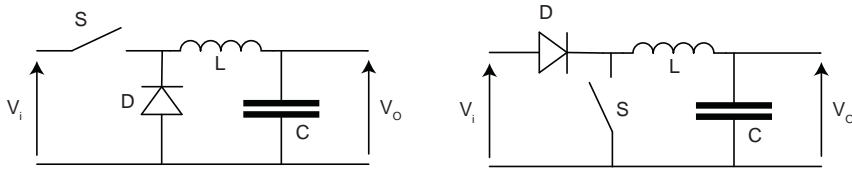
Figure 2.11.
Basic topology of a boost (left hand side) and buck (right hand side)
converter.

2.6.3.2. DC/AC inverter

In order to integrate a photovoltaic device into the electrical grid, one has to meet
the specific a.c. frequency and voltage for the associated region. To convert the
d.c. output to a sinusoidal a.c. signal an inverter is needed. Basically there are
three types of inverters [19, p. 108]. *Variable frequency inverters,* which are used
almost exclusively in PV pumping systems. And *fixed frequency converters* which
are subdivided into *self commutating* and *line commutated.* Self commutating
fixed frequency converters are able to turn on and off under internal control.
They are mostly used for smaller systems up to several kW_p.

Line commutated inverters on the other hand use thyristor switches and require
an altering load voltage from an external source to turn the switches off. These
are used for larger systems.

The most basic inverter topology just produces a square voltage waveform that
is not suitable for most appliances. To overcome this problem sinusoidal pulse
width modulation is used. Here the switches operate at a frequency usually above
20 kHz [19, p. 105] and the duty ratio δ_c is varied to produce an approximate
sine curve as needed in the grid.

2.6.3.3. Maximum power point tracker

A MPP tracker controls the current and the voltage and adjusts the duty cycle
of the converter accordingly to ensure maximum power output. Among the many
algorithms that have been proposed, two are predominantly applied to track the
maximum power point. The *perturbation and observation* (P&O) method and the
incremental conductance (IncCond) method. The P&O method is very popular
due to its easy implementation. In its simplest realization the MPP tracker works
by periodically incrementing or decrementing the solar array voltage V_i. If a given
perturbation leads to an increase of the power output, the subsequent perturbation
is directed towards the same direction, whereas a decrease of the power output

results in a change of direction. The P&O algorithm compares only two points, the current operation point and the subsequent perturbation point, to decide whether to decrease or increase the solar array voltage V_i. This normally results in an oscillation around the MPP, under constant incident sunlight.

The IncCond method works by comparing the incremental conductance $\mathrm{d}I/\mathrm{d}V$ and chord conductance I/V. It deploys the fact that at the MPP, the derivative of the output power with respect to its voltage is zero $\mathrm{d}P_{out}/\mathrm{d}V_{out} = 0$ [5].

In both cases a feed back loop determines the adjustment of the duty cycle. These feed back loops can be disturbed by a distortion of the monitored current voltage signals [32].

3. Experimental setup outdoors

In the outdoor measurements a case study of the effect of wind induced vibration on the performance of a solar module, was conducted. It was investigated, if there is a direct correlation between wind acceleration and distortion signals, which could be verified in a statistical analysis. Additionally the effect of the angle position of the solar module with respect to the sun's position, was examined.

3.1. Basic experimental setup

The outdoor investigations were done in central Vienna at the roof top of the institute building. Table 3.1 summarizes the local position.

As rack a two axis gimbal mount originally designed for solar irradiance measurements was used, which allowed varying the inclination manually with a simple lever lock. The orientation from North, ψ_0 was kept constant at 180.7 deg in our experiments. The rack with the module can be seen in figure 3.1, the iron shadow ring, originally mounted for diffuse radiation measurements, was removed after the picture had been taken.

Latitude	48.22165° N
Longitude	16.3558° E
Altitude	202 m

Table 3.1.
Location of experimental setup determined by GPS.

In the outdoor setup a 10 W$_\text{p}$ flat solar module of multicrystalline silicon cells was used. The panel is specified for 17 V operation with an output current of 0.6 A which would require a 28 Ω load impedance, for optimum power output. The module was operated either with a 21 Ω/25 W resistor monitoring the photo-current which remains close to short circuit current conditions at all intensity levels. Alternatively the module was connected to an *Agilent Technologies* 50V/3A power supply module (*N6762A*) inserted in a N6705A frame with integrated measurement capabilities for voltages and currents up to sample rates of 10 kHz. The power supply was capable to serve as adjustable sink and made it possible to carry out measurements at different operating points.

Figure 3.1.
Solar module mounted on a two axis gimbal mount (left hand side). Backside of the solar module with the geophone mounted horizontally (right hand side).

3.1.1. Additionally recorded parameters

- The incident intensity was recorded by means of a *Kipp & Zonen pyranometer type CM6B*.

- The wind speed in the range between 1.5 m/s and 15 m/s by an anemometer from *Wilh. Lambrecht*.

- The displacement was recorded via an encapsuled three axis geophone from *Mark Products Inc.*

The geophone was fixed horizontally on the rack as can be seen on the right side in figure 3.1. Horizontal and vertical geophone velocities were recorded simultaneously with the light generated current at sample rates of at least $1\,\mathrm{kSs}^{-1}$. The velocities were converted to displacement coordinates, Δx, Δy and Δz by numerical integration. The x-axis was east-west oriented, the y-axis north-south and the z-axis perpendicular in vertical direction.

The specifications of the geophone for the three different axis are identical and as follows: The sensitivity is $26.9\,\mathrm{V}\,(\mathrm{m/s})^{-1}$, the frequency limit is $4.5\,\mathrm{Hz}$ and the slope at lower frequencies is $12\,\mathrm{dB/oct}$.

3.2. The yaw pitch roll frame of reference

In section 2.4 the current position of the sun is described via the solar elevation α and the azimuth τ. In order to examine the variation of the panel's orienta-
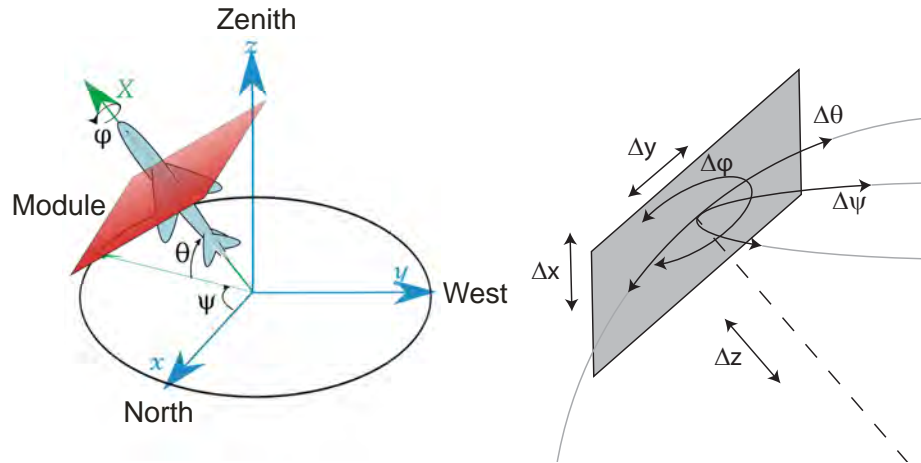
Figure 3.2.
The yaw pitch roll model is well known in aeronautics. In red shadings the position of the solar panel, with respect to the three angles is shown on the left hand side (rework from www.wikipedia.org). On the right hand side the Cartesian coordinate inertial system of the solar panel is shown.

tion towards the sun and thus the intensity variations of the incident sun light on the module's surface it is more convenient to introduce a new set of angles. A transformation in rotation angles in analogy to the yaw-pitch-roll model used in aeronautics seems favorable. The three angles defined by the model are ψ, Θ and φ as depicted in figure 3.2. Where ψ is the horizontal angle from north. The pitch angle Θ is the inclination from the horizon and may not be confused with the definition of the tilt angle commonly used in photovoltaic terminology which is defined by the angle between the horizontal plane and the module's plane. The pitch angle Θ equals the angle between the surface vector and the horizontal plane. The tilt angle therefore relates to the pitch angle by $90 \deg -\Theta$. The roll angle φ describes a rotation coplanar to the module. Therefore at least for flat plate modules φ should not contribute to intensity variations caused by the module's displacement. During our experiments the inclination Θ_0 was varied between $90 \deg$ (tilt angle=$0 \deg$, horizontal module position) and $5 \deg$ (tilt angle= $85 \deg$, steep module position). In figure 3.2 on the right hand side the Cartesian coordinate system, as defined by the geophone axis, and the yaw pitch roll frame of reference is depicted. The transformation is given by equations 3.1 - 3.4.

$$(x + \Delta x,\, y + \Delta y,\, z + \Delta z) = (x, y, z) R_\psi R_\Theta R_\varphi \tag{3.1}$$

$$R_\psi = \begin{pmatrix} \cos\psi & \sin\psi & 0 \\ -\sin\psi & \cos\psi & 0 \\ 0 & 0 & 1 \end{pmatrix} \tag{3.2}$$

$$R_\Theta = \begin{pmatrix} 0 & 0 & 1 \\ \cos\Theta & \sin\Theta & 0 \\ -\sin\Theta & \cos\Theta & 0 \end{pmatrix} \tag{3.3}$$

$$R_\varphi = \begin{pmatrix} \cos\varphi & \sin\varphi & 0 \\ -\sin\varphi & \cos\varphi & 0 \\ 0 & 0 & 1 \end{pmatrix} \tag{3.4}$$

Assuming the mounting rack to be a rigid body, solely the horizontal displacement given by Δx and Δy is independent whereas the vertical component Δz is a function of Δx and Δy. Consequently calculating the variation in orientation ($\Delta\psi$) and inclination ($\Delta\Theta$) further simplifies.

3.3. Properties of the mounting construction

Prior to evaluating data at different weather conditions, mechanical vibrations were introduced by applying short manual forces to the mounting rack. This was done by simply pushing or pulling the rack on a clear sunny day during periods where the wind velocity was below detection limit. Knowing the horizontal displacement and the sun's position, the effect of varying misorientation of the module's surface relative to the geometrical path of sun rays and thus the variation of the incident light intensity, P_{inc} on the module's surface were calculated as well as the vertical displacement for the rigid body simplification. A comparison between the measured and calculated values of Δz shows that the experimentally observed elongation always was at least one order of magnitude larger than calculation. That indicates that the rigid body assumption is not justified. None the less a comparison of the model calculations of oscillating P_{inc} and the recorded module's current I_{module} qualitatively agree fairly well in several cases. After the application of a short force in north – south direction the rack is horizontally displaced at similar amplitudes as well in N-S as in E-W direction. The magnitude was generally less than $2\,\text{mm}$ in one direction. The rack oscillates at frequencies between $4\,\text{Hz}$ and $5\,\text{Hz}$. The frequency shifts with the center of mass of the system, which depends on the adjusted inclination, since the construction is not well balanced in the center of the gimbal axis. The frequency of the E-W displacement always differed somewhat from the frequency of the N-S displacement resulting in a rather complex horizontal trace of the total displacement. The observed
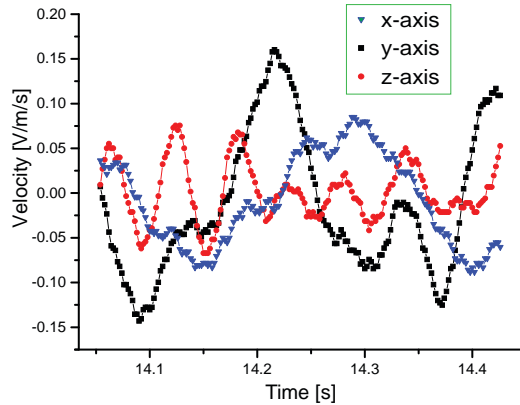
Figure 3.3.
A half second long sample from the results of the three-axis geophone.

damping time constant typically was about 4 s. Vertical displacement oscillations occurred at much higher frequencies of 16 Hz to 18 Hz.

Additionally geophone data was recorded during the course of a day, where the solar panel was exposed to ambient conditions. 30 seconds long sample measurements where recorded every 10 minutes. The results are shown in figure 3.3. The graph is derived from a 30 second long sample measurement. The wind speed during the measurement had an average of roughly 6 m/s.

In order to extract the measured photo-current oscillations in time intervals of 2 s in a first step a linear fit accounting for the current d.c. offset value of the photo-current, I_{DC}, and potentially present slow variations of sun light intensity was performed. The residual of the photo-current, I_{AC}, was Fourier transformed and the amplitude spectra were compared with the displacement oscillations. Within the uncertainties, due to changing ambient conditions during the various experiments, the magnitude of the a.c. photo-current increases linearly with the amplitude of horizontal displacement. At different incident light intensities the relative a.c. photo-current defined as the ratio $I_{rel} = I_{AC}/I_{DC}$ remains almost constant for similar excitation conditions of the mounting rack.

3.3.1. Model calculations

Model calculations of the variation of the incident light intensity P_{inc} were carried out using the measured horizontal displacement amplitudes and compared with the relative changes in the module's photo-current. Beside the simplifications of the model described above it shall be noted that the calculation accounts solely for the direct direct radiation B with a geometrical light pass. Since for our load resistor $I_{module} \approx I_{sc} \propto P_{inc}$ is valid in all cases the relative amplitudes as defined

here are compared:

$$P_{rel} = \frac{P\left(\psi + \Delta\psi\left(t\right), \Theta + \Delta\Theta\left(t\right)\right) - P\left(\psi_0, \Theta_0\right)}{P\left(\psi_0, \Theta_0\right)} \qquad (3.5)$$

$$\begin{aligned} \Delta\psi\left(t\right) = & \quad f\left(\Delta x\left(t\right), \Delta y\left(t\right)\right) \\ \Delta\Theta\left(t\right) = & \quad g\left(\Delta x\left(t\right), \Delta y\left(t\right)\right) \end{aligned} \qquad (3.6)$$

ψ_0 and Θ_0 are the static, undisturbed angles of the module's orientation. The functions f and g are the inverse operations to equation 3.1. Subsequent measurements with different module inclination were carried out using manual forces in N-S direction and measured and calculated magnitudes of the oscillations were compared (figure 3.4).

3.4. Outdoor results for the angle dependency

The measurements were done at the 20th August at about 16:30 in the afternoon where the misorientation of the module to the incident sun rays was between 30 deg and 75 deg depending on the inclination shown in figure 3.4 as dashed line (right axis). The smallest deviation in the module's orientation would be for a tilt angle of 17 deg. For $\Theta_0 < 45$ deg calculations (continuous line in figure 3.4) and experimentally observed current oscillations (symbols) are in fair agreement. However calculations result in significantly too high values at low misorientation angles most likely due to the unjustified assumption of a rigid body construction. Although the relation between misorientation angle and the magnitude of distortion can be clearly seen by comparing the tendency of the symbols with the dashed line in figure 3.4 obviously it is not a simple linear dependence. A little surprising is the circumstance that the smallest current amplitudes do not occur at minimal misorientation. The minimum in the first case was experimentally observed at an inclination angle of 60 deg, whereas the least misorientation would be around 70 deg of inclination. For larger misorientation the distortion increases stronger than linear.

3.4.1. Statistical evaluation of the outdoor results

On several days with different weather conditions, as by means of wind speed and cloud cover, current oscillations, vibrations and wind velocities were monitored during the day at sampling rates of 10 kSs^{-1}. In the period of observation the highest recorded wind speeds were a little more than $15\,\text{ms}^{-1}$. The cloud cover ranged from dense rain clouds to clear blue sky. On average the observed displacement amplitudes and corresponding photo-current oscillations with respect to the panel orientation towards the sun scale directly with the average wind speed. Since
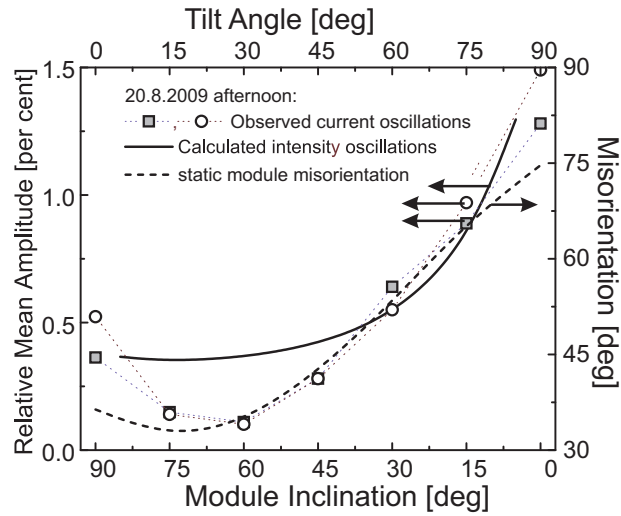
Figure 3.4.
Dependence of the magnitude of vibration induced current oscillations on the
module's inclination.

it is assumed that vibrations are preferentially introduced by a sudden change in
wind speed the acceleration obtained from the wind speed recordings were cor-
related with the appearance of high displacement and photo-current oscillations.
The response time of the anemometer was determined to be $0.75\,\mathrm{s}$ which seems to
be sufficiently fast to obtain acceleration in real time. However only in a few out
of many examined cases a doubtless coincidence between wind acceleration and
rack vibrations could be resolved. One major reason presumably is the distance
between the location of the rack and the position of the anemometer of more than
5 m, which was necessary due to the limited cable length between anemometer
head and electronic unit, which was placed in the house. Therefore we currently
restrict the observations on statistical data evaluation.

A typical example is given in figure 3.5 which shows the number of occurrences
where the amplitude at a distinct frequency in the monitored frequency range of
$2.5\,\mathrm{Hz}$ to $5\,\mathrm{kHz}$ is the largest. Two results are shown for similar ambient conditions
but different inclination angles, 45 deg and 15 deg respectively. In order to ease
the comparison the occurrence count was normalized to the total number of sam-
ples. Although the wind speeds on average and on peak are low in about $50\,\%$ of
all events the largest amplitude was seen at the typical vibration frequency of $5\,\mathrm{Hz}$.
The peaks above $100\,\mathrm{Hz}$ were identified to arise from electromagnetic distortion
caused by a large cooling unit near by. Although both distributions are similar
the magnitudes of the largest oscillations differ significantly. For an inclination of
45 deg a peak value of $0.76\,\mathrm{mA}$ or $0.13\,\%$ was recorded. During the observation
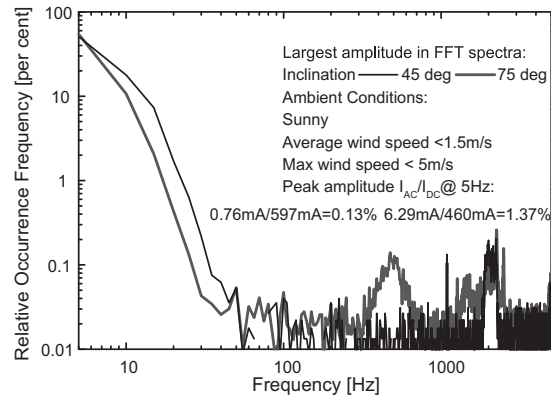with an inclination of 15 deg where the module was mounted steeper than before

Figure 3.5.
Example of statistical evaluation. It shows the relative number of
occurrences, where the largest amplitude was observed at a certain frequency.

the largest current amplitude was $6.29\,\mathrm{mA}$ or $1.37\,\%$ which is in agreement with
our experiments on the inclination dependency of the vibration effect.

4. Laboratory measurements

The goal of the laboratory measurements was to show the dependence of deflection, angle of misorientation and different interconnections, on the magnitude of the superimposed a.c. noise, for a specific setup. In section 4.1 the fundamental setup, of all laboratory measurements conducted, will be outlined. In section 4.2 the deflection characteristics of the vibrating table were examined.

In section 4.3 two solar cells were mounted on the vibration table and operated in series and in parallel. A resistor array was constructed, so the load resistance could be varied. Additionally current voltage curves of the solar cells have been measured. This was done to asses at which load resistance the a.c. noise peaks and how this relates to the MPP. The results obtained in this section are supplemented by the results of chapter 5.

In Section 4.4 the angle of the solar miniature module with regard to the light source, has been varied. It directly relates to outdoor experiments in section 3.4.

4.1. Basic measurement setup

The vibration table mainly consists of a subwoofer[1] with a free air resonance of $32\,\mathrm{Hz}$, which is quite close to the very low frequency range under observation. A detachable acrylic plate was fixed on top of the subwoofer. Onto that acrylic plate a holder for the solar cells was attached. The holder allows changing the angle of misorientation determined by the cell's surface vector and the optical axis of the light source. This angle was later varied to determine the angle dependency of the distortion signal (see section 4.4). The different solar cells can be fixed onto the holder via a hook and loop fastener.

A schematic of the most basic setup is illustrated in figure 4.1. The vibration table is excitated sinusoidally through the function generator in the direction of the z-axis. The solar cell is connected to an impedance R_{Load}, which is not included in figure 4.1. The impedance is either a resistor, or a switchable resistor array (see section 4.3.2).

The function generator, determining frequency and excitation amplitude and the lock-in amplifier, for detecting the a.c. component of the test unit's output both were connected to a personal computer. The setup was controlled via NI LabVIEW 7.1 [15]. A picture of the setup is shown in figure 4.2.

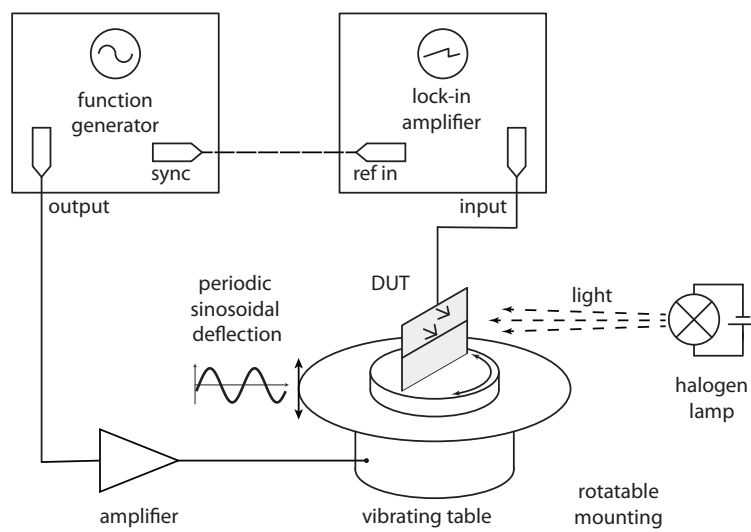[1]124SX Xtreme Subwoofer, W_p :400 Watt, W_c :200 Watt

Figure 4.1.
Most basic measurement setup, with a lock-in amplifier, a function generator,
an amplifier, the vibration table with a solar cell mounted on it and a
halogen lamp.
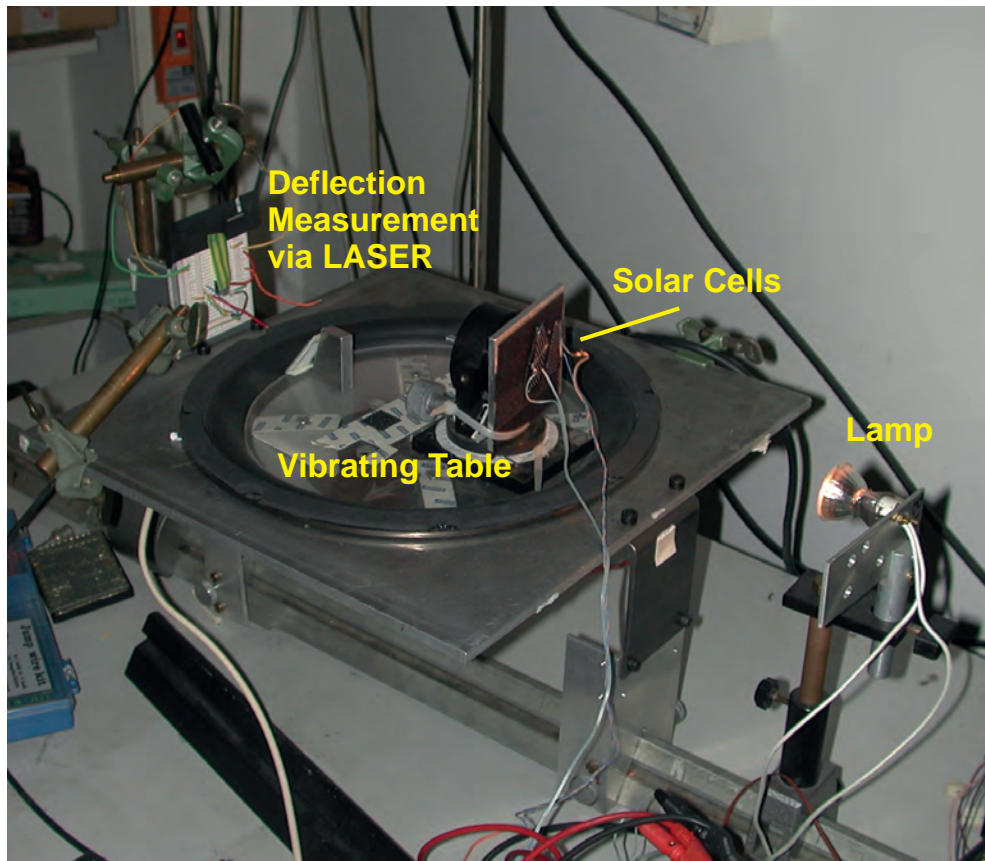
Figure 4.2.
Experimental setup.

Figure 4.3.
On the left hand side the amorphous silicon solar miniature module is shown.
On the right hand side the two small multicrystalline solar cells are fixed on
the holder on the vibration table.

4.1.1. Instruments and devices under test

As lock-in amplifier the model *SR530* from *Stanford Research Systems* was used.
The lock-in amplifier has a maximum time constant of $100\,\mathrm{s}$ which was used for
most measurements. To amplify the signal of the function generator a *Kepco*
power supply amplifier, which drives the subwoofer, was used. The lock-in amplifier and the function generator were both connected via GPIB to a personal
computer. As light source a halogen lamp, operated with a $12\,\mathrm{V}$ power supply,
was used.

Additionally the *National Instruments USB-6009* and the *National Instruments
Elvis* were used for the resistor array control. The *NI Elvis* has six differential
analog input (AI) channels available, one of which was used to acquire the data
from the linear sensor array, for the deflection measurement described in section
4.2. On top of the *NI Elvis* is a breadboard which was used for building the
resistor array described in section 4.3.2. To gate the resistor array the *NI USB-6009* was used. It has 12 digital I/O pins, 8 analog input and 2 analog output
pins. A schematic side view of it can be found in Fig. 4.9. For the deflection
measurement a *TSL1401 linear sensor array* that consists of 128 photo diodes
arranged linearly was used. Each element measures $63.5\,\mu\mathrm{m}$ (H) by $55.5\,\mu\mathrm{m}$ (W)
with $63.5\,\mu\mathrm{m}$ center-to-center spacing (see section 4.2).

Experiments where carried through, either with an amorphous silicon miniature
module or with two multicrystalline cells, as devices under test. They can be seen
in figure 4.3. The a-Si module has a width of $57\,\mathrm{mm}$ and a height of $50\,\mathrm{mm}$.
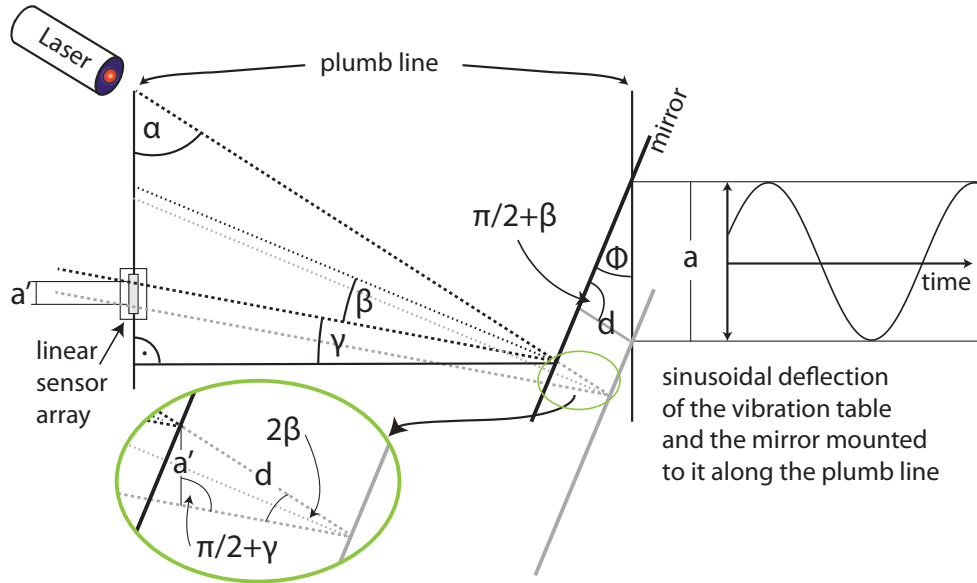
Figure 4.4.
Schematic view of deflection measurement construction.

4.2. Deflection characteristics of the vibration table

In this section the deflection of the vibrating table, with respect to the frequency has been determined. The electrical amplitude of the frequency generator has not been changed throughout the measurement and will be refered to as default amplitude. Hence the frequency with the maximum deflection of the subwoofer's membrane for the default amplitude could be determined. The electrical excitation amplitude was kept constant for all subsequent measurement runs.

To determine the excitation at different frequencies, a laser and the linear sensor array TSL 1401 were fixed beside the vibration table, so they would not be affected by the vibration directly. The mirror on the other hand, was fixed directly on the vibration table. The laser beam was directed, in a manner so that it would be reflected by the mirror and then impinge on the linear sensor array. The setup of the measurement can be seen in figure 4.4.

To determine the deflection of the vibration table a, one first has to derive the ratio a/a'. Where a' is the distance on the linear sensor array, between the two points where the laser beam hits the array, when the vibration table is deflected by an amplitude a.

Additionally the angles Φ and α are required. To measure them, a pendulum was used as a plumb bob together with a digital camera. The plumb line is a vertical
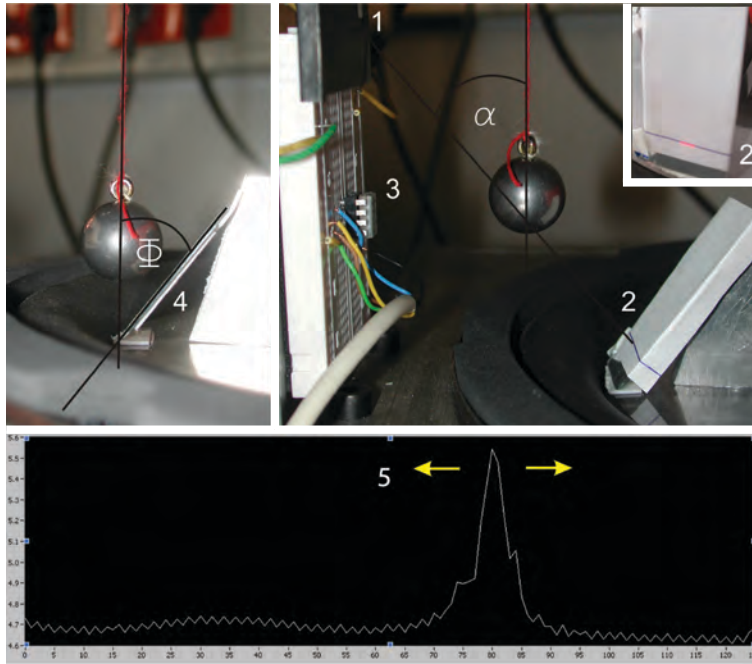
Figure 4.5.
Schematic of the line array measurement: 1. Aperture for laser beam 2.
Mirror with paper on it for better detection of laser beam for the calibration.
3. line array 4. Mirror 5. LabVIEW output.

reference line and the deflection of the vibration table can be assumed to be along the plumb line.Φ is the angle of the mirror, in relation to the plumb line and α the angle of the path of the laser beam, also in relation to the plumb line, as can be seen in figure 4.4.

The pendulum suspension was placed directly over the deflection measurement setup. The photos were taken from a digital camera fixed to a tripod several minutes after any perceptible movement of the pendulum had stopped. To minimize the error of parallax, the weight of the pendulum has been placed to intersect the path of the laser beam. In figure 4.5 we can see the results of the angle measurement. An aperture has been used to narrow the laser beam, so that only one photo diode gets the maximum light intensity at a time. This worked very well, as can be seen at the output of the LabVIEW program shown at the bottom of figure 4.5. It shows the line of 128 photodiodes on the x-axis and the respective intensity of the reflected laser beam on the y-axis. The peak is shifting on the x-axis when the vibration table is deflected. The x-axis units are the photo diodes, each $63.5\,\mu$m apart, while the y-axis unit is in volts. To calibrate the setup a paper has been placed on the mirror, to make the laser beam visible.

We can see α on the upper right hand side of figure 4.5. The angle can be determined from the lines plotted in *Adobe Illustrator CS5*. The results are $\alpha = 0.715\,\text{rad}$ and $\Phi = 0.697\,\text{rad}$, they are also summarized in table 4.1

The position of the reflected laser beam is monitored by the TSL1401 linear sensor array that consists of 128 photo diodes. The pixels measure $63.5\,\mu\text{m}$ (H) by $55.5\,\mu\text{m}$ (W) with $63.5\,\mu\text{m}$ center-to-center spacing and $8\,\mu\text{m}$ spacing between pixels, where the width is measured in the direction of the line of the photo diodes. So the physical resolution of a' is $63.5\,\mu\text{m}$.

To obtain the ratio a/a' from these three variables (a', Φ, α), it is helpful to introduce some dependent variables (β, γ, x):

The angle β, is the angle between the laser beam and the line perpendicular to the mirror. The angle γ, is the angle between the horizontal line (perpendicular to the plumb line) and the laser beam reflected back from the mirror, as shown in figure 4.5. From figure 4.5 we derive:

$$
\begin{aligned}
\beta + \gamma &= \Phi \\
\pi/2 &= 2\beta + \gamma + \alpha
\end{aligned}
\tag{4.1}
$$

Consequently:

$$
\begin{aligned}
\beta &= \pi/2 - \alpha - \Phi \\
\gamma &= 2\Phi + \alpha - \pi/2
\end{aligned}
\tag{4.2}
$$

By introducing d as the additional distance the laser beam has to travel, when the mirror is moved down by a, we can use the law of sines, to determine a/a'.

From the upper triangle shown in figure 4.5, we derive:

$$
\frac{d}{\sin(\Phi)} = \frac{a}{\sin(\pi/2 + \beta)}
\tag{4.3}
$$

From the lower magnified triangle, we now derive:

$$
\frac{d}{\sin(\pi/2 + \gamma)} = \frac{a'}{\sin(2\beta)}
\tag{4.4}
$$

By equalizing these two equations we get:

$$
\frac{a}{a'} = \frac{\sin(\pi/2 + \beta)}{\sin(\Phi)} \frac{\sin(\pi/2 + \gamma)}{\sin(2\beta)}
\tag{4.5}
$$

No we substitute the angles with eq. 4.2:

$$
\frac{a}{a'} = \frac{\sin(\pi - \alpha - \Phi)}{\sin(\Phi)} \frac{\sin(2\Phi + \alpha)}{\sin(\pi - 2\alpha - 2\Phi))}
\tag{4.6}
$$

α	$0.715\,\text{rad}$
Φ	$0.697\,\text{rad}$
$\frac{a}{a'}$	4.22077
center to center spacing of line array	$0.268\,\text{mm/point.}$

Table 4.1.

Angles and proportion derived from figure 4.5 using equation 4.7.

$$\frac{a}{a'} = \frac{\sin\left(\alpha + \Phi\right)}{\sin(\Phi)} \frac{\sin\left(2\Phi + \alpha\right)}{\sin\left(2\alpha + 2\Phi\right))} \tag{4.7}$$

Now we have everything we need to determine a/a'. The results are shown in table 4.1.

4.2.1. Measurement and results

For the measurement of the deflection, the excitation frequency was varied from 0.5 to $12\,\text{Hz}$ in steps of $0.25\,\text{Hz}$, at the default amplitude. Each frequency was recorded for 90 seconds and analyzed via a NI LabVIEW virtual instrument, based on the parameters given in table 4.1. The virtual instrument then calculated the peak-to-peak amplitude. Data recorded within 3 seconds after the switch to a higher frequency was not used for the analysis, to allow the system to adjust to the new frequency. Test runs were taken with both, the amorphous silicon solar module and the single cells mounted to the table, to see if there are any differences in the amplitude, arising from the different mass of the vibrating plate. However these differences were not distinguishable from the statistical error occurring, under exactly the same setup. So for the statistical analysis three measurements, with the amorphous silicon module mounted, have been recorded. In figure 4.6 we can see the mean value of the deflection for all three runs. The standard deviation always remains below 2.1 %. We can see a clear peak at about $8\,\text{Hz}$, where the peak-to-peak deflection is about $4.5\,\text{mm}$ for the standard excitation amplitude.

4.3. Varying load resistances and two different circuit arrangements

In this chapter the two small multicrystalline solar cells (see section 4.1.1) were mounted on the vibration table and operated either series or parallel, to asses at which load resistance the a.c. signal peaks and how this relates to the MPP. To accomplish this, current voltage curves of the solar cells were recorded (section 4.3.1). To make sure, that the effect of electromagnetic interferences caused by

Figure 4.6.
Deflection measurement of the vibrating table.
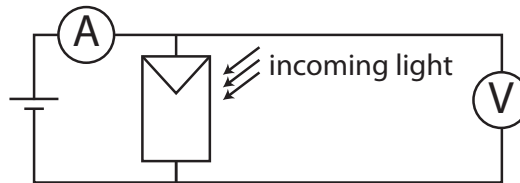
Figure 4.7.
Setup for acquiring the current voltage curves.

the system, don't distort the results an error measurement was conducted (section 4.3.3). To vary the load resistance, a resistor array was constructed (section 4.3.2).

4.3.1. Current voltage curves

To obtain the maximum power point and the associated load resistance R_{load} under illumination characteristic curves were recorded.

The basic setup of the measurement can be seen in figure 4.7. The resulting $I(V)$ and power curves for the two single solar cells are shown in figure 4.8. The curve for the a-Si module was used in figure 2.8 of section 2.5.1, to illustrate the MPP and the fill factor.

In figure 4.8 and figure 2.8 the voltage and the current are given variables, which could be obtained directly from the measurement. The algebraic sign of the current I was changed for illustration purposes in the $I(V)$ curves of all cells. The power curve was then calculated from the obtained $I(V)$ curves where the original value of I was used to calculate P, using $P = U \cdot I$.

	Voltage [V]	Current [mA]	Power [mW]	Load [Ω]
a-Si module	2.35	2.67	6.27	881.56
cell #1	0.39	15.2	5.9	25.47
cell #2	0.36	21.4	7.7	16.5

Table 4.2.
Electrical parameters for the devices under test at the maximum power point, when they are illuminated.
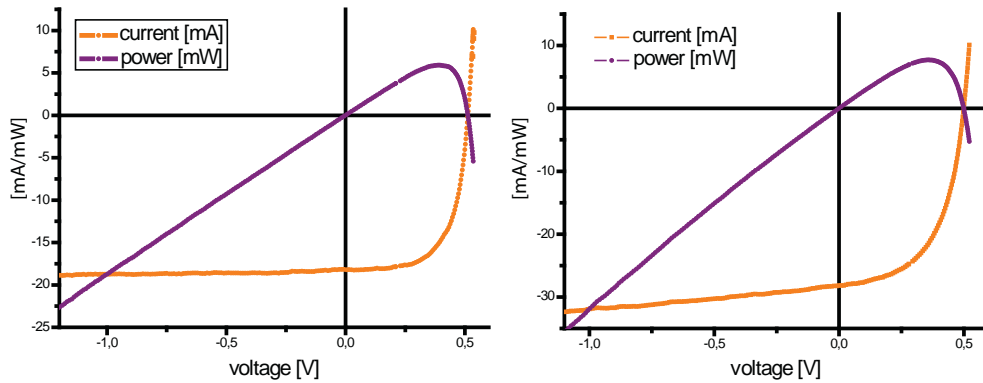
Figure 4.8.
Characteristic curves for the two multicrystalline solar cells. The $I(V)$ curve is in orange and the $P(V)$ curve in magenta. Single cell #1 is on the bottom left and cell #2 on the bottom right. All measurements were taken under illumination.

The results at P_{max} are shown in table 4.2.

The operating points of the illuminated solar cells will be of further interest when discussing the results of the resistance measurement in section 4.3.4 and in chapter 5.

4.3.2. Resistor array architecture

To test the different solar panels under variable load conditions a circuit has been designed. Eight resistors were connected in series and can be bypassed individually by 8 relays, as shown for the first two resistors in figure 4.9. The relays were controlled by the digital out ports of the NI USB 6009. Each digital outport was connected, through a pre-resistor, with the base of an NPN transistor (BC548B). The emitter was connected to the ground and the collector to the relay.

Eight resistors that can be switched on and off independently allow $2^8 = 256$
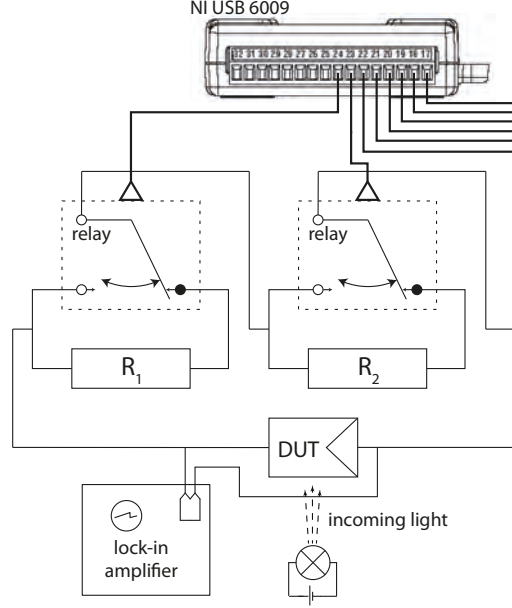
Figure 4.9.
Schematic circuit of the resistance variation.

	R_1	R_2	R_3	R_4	R_5	R_6	R_7	R_8
resistor [Ω]	6.8	15	27	56	100	180	330	680

Table 4.3.
Nominal values of the resistors used in the resistor array measurement.

different configurations. It has been tried to use a set of resistors, that closely matches the condition $2R_i = R_{i+1}$, so the total load resistance R_{tot_k} for the configuration k equals:

$$R_{tot_k} = \sum_{i=1}^{8} c_{k_i} R_i \qquad (4.8)$$

with $k\epsilon\{0, 1, ..., 255\}$ and $c_{k_i}\epsilon\{0, 1\}$ the eight values for c for each k are derived from a Boolean array (or bit array) where each k is associated with the corresponding 8 bit array in the dual basis. The values of R_i are listed in table 4.3. This allows to vary R_{load} between $\sim 0\,\Omega$, where all relays are open to nearly $1400\,\Omega$, where all relays are closed, which exceeds all maximum power point values for R_{load} in table 4.2.

A comparison between calculated and measured R_{tot} was made. For the latter an external current source had to be connected (for this the Keithley 224

programmable current source was used) to the resistors, while simultaneously measuring the voltage. The current source was operated at $100\,\mu\mathrm{A}$ and a *VI* programmed with NI LabVIEW was used. The measured resistance matched the theoretically calculated resistance within an error range of $\pm 2\,\%$.

4.3.3. Error due to the electromagnetic interference of the setup

The a.c. voltage for most measurements is usually in the regime of millivolts. Due to this small value, the electromagnetic radiation emitted by the setup could be distorting the measurement. Especially radiation emitted by the self constructed vibrating table might induce additional current to the solar cell's interconnection. The lock-in amplifier would not help to supress the noise signal in this case.

To asses the effect a piece of acrylic glass was mounted aside the table with a double socket. The solar module could be fixed to the acrylic glass with a hook and loop fastener, just like on the usual mount. This arrangement kept the solar module still, but parallel to the vibrating mounting unit at just about $1\,\mathrm{cm}$ distance, close enough to pick up the electromagnetic field generated by the vibration table during operation.

A test run was taken with the amorphous silicon module under the same parameters as the one taken in section 4.3.4. The resulting curve roughly matched the outcome of section 4.3.4. However the signal remained always well below $1\,\mu\mathrm{V}$, or below $1\,\text{‰}$ of the a.c. signal. Therefore the effect can be neglected.

4.3.4. Measurements and results

These measurements were undertaken with the two small multicrystalline silicon solar cells under illumination. The basic test setup is illustrated in figure 4.1 and outlined in section 4.1. The angle of misorientation ν as explained in section 4.4 was set to 0, (the surface is oriented perpendicularly to the optical axis).

The cells were operated singularly, series connected and parallel connected, not changing anything about the experimental setup, lest the interconnection. Figure 4.10 shows the results of a measurement, realized via the lock-in amplifier. The constant frequency for this measurement was $8.68\,\mathrm{Hz}$. According to the data from section 4.2.1 this corresponds to a deflection of $4.3\,\mathrm{mm}$. The time constant of the lock-in amplifier was set to $100\,\mathrm{s}$.

For the interpretation of the results a comparison with the characteristic current voltage curves obtained in section 4.3.1 is useful. Table 4.2 shows that the resistance associated with the maximum power point is $25.47\,\Omega$ for cell #1 and $16.5\,\Omega$ for cell #2. The values for the resistance at the maximum of the transient a.c. signal acquired in this measurement are $R = 28.9\,\Omega$ for cell #1 and $R = 18.9\,\Omega$
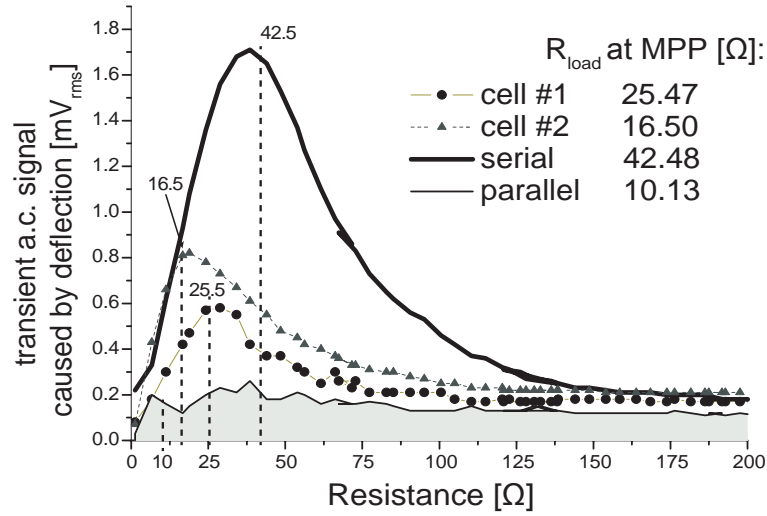
Figure 4.10.
Amplitude of transient a.c. signal, derived from a lock-in amplifier. The Measurement was done at 8.68 Hz excitation frequency. The dashed lines show R_{load} for the maximum power point of a given setup. The resistance values are derived from table 4.2.

for cell #2. The maximum of the transient a.c. signal lies close to the maximum power point of each cell.

Further in figure 4.10 we can see, that the two cells connected in series yield a signal which at its peak is greater than the sum of the maxima of the two transient a.c. signals of both cells. The expected peak for the two cells connected in series would be at $R_{\#1} + R_{\#2} = 41.97\,\Omega$, which again lies very close to the maximum of the transient a.c. signal.

For the two cells connected in parallel the resistance at the maximum power point would be $(1/R_{\#1} + 1/R_{\#2})^{-1} = 10.01\,\Omega$. However the parallel connected cells barely seem to be affected by the disturbances at all. This can be explained by the fact that a single solar cell basically behaves like two solar cells connected in parallel, with their cumulative areas determining the current and their voltage being constant. This can lead to the effect that disturbances that might sum up in a series connected setup, cancel out in a parallel connected setup. The impact of this effect might have been enforced by the nature of our light source. The light source has a fixed pattern of inhomogeneity, which alternately covers up different parts of the solar cells. This doesn't model ambient conditions very accurately, so the extent of this effect probably is overrepresented. However at the laboratory results in section 5.4 the distortion for a parallel setup was still less than half of the series setup with regard to the power and it can be definitely concluded, that the distortion effect of parallel connected solar cells is greatly reduced.

By comparing the results of the a.c. measurement with the static d.c. values from table 4.2 we can assess the fraction of the distortion of the resulting voltage. However these quantitative results are constrained to our setup and are just mentioned for the sake of completeness. Additionally they were measured with a very long time constant ($\tau = 100\,\text{s}$), hence with a very narrow bandwidth which diminishes the signal's magnitude (see section 5.2). Lastly we are comparing the root mean square results from the measurement with a d.c. values. The maximum of distortion $V_{rms,max}$ for cell #1 is $0.58\,\text{mV}$ with $R = 28.9\,\Omega$ and for cell #2 $V_{rms,max}$ it lies at $0.82\,\text{mV}$ with $R = 18.9\,\Omega$. Compared with the voltage of this cell at the MPP we obtain: $V_{rms,max}/V_{MPP} = 1.49\,\text{‰}$ and for cell #2 $V_{rms,max}/V_{MPP} = 2.28\,\text{‰}$.

These results are just approximated values for a specific setup with the restrictions mentioned in the last paragraph. Furthermore the results obtained in this section are not directly comparable to the outdoor results obtained in section 3.4, since in the outdoor results, the ratio of the current noise to the d.c. current signal was measured and not the voltage ratio.

4.4. Angle dependency

In order to supplement the results of section 3.4, the angle dependency of the a.c. signal, has been conducted for the specific setup, in the laboratory, as well.

The measurements have been conducted with the amorphous silicon module, and the load resistor $R_L = 1\,\text{k}\Omega$ was kept constant for the whole measurement. On the left side of figure 4.11 the basic principle of the setup is illustrated. The angle of misorientation ν, is defined as the angle between the surface vector of the solar module and the shortest connecting line between the rotational axis and the light source. The angle was varied manually.

In section 3.2 the yaw pitch roll model was introduced to describe the behavior of a solar panel with three degrees of freedom in ambient conditions. The change $\Delta\nu$ of the angle ν as shown in figure 4.11 corresponds to the change of the yaw angle $\Delta\psi$, when the pitch angle Θ and the roll angle φ are set to zero.

Unfortunately with this setup it was not possible to emulate a variation of the misorientation of the angle itself. As can be seen in figure 4.11, the axis of deflection corresponds to the rotational axis of the solar cell.

As discussed in section 2.4.5, the incoming light flux on a solar panel in ambient condition has three components. The direct beam radiation B, the diffuse radiation D and the albedo radiation R. All of these are dependent on the inclination of the solar module κ, and the relative position of the sun towards the module. The diffuse radiation $D(\kappa)$ can be assumed to be constant [19]. The impact of the albedo radiation $R(\kappa)$ is usually small since the reflectivity of most surfaces is
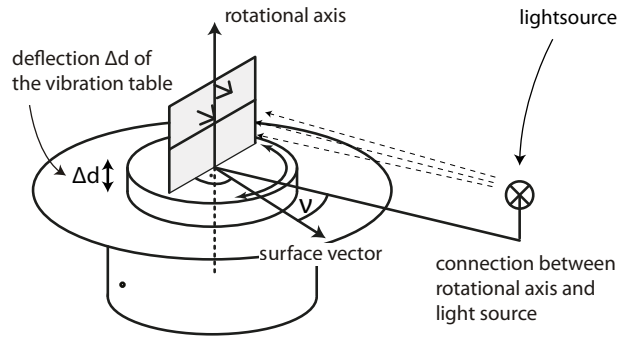
Figure 4.11.
Schematic of the angle dependency measurement with a depiction of the
angle of misorientation ν,

rather low. In these cases the presented models won't describe the radiation behavior very well. Only the direct radiation $B(\kappa)$ will be taken into account here, since it is the dominant source of light for most cases and strictly anisotropic.

4.4.1. Systematic error

Our source of illumination is a halogen lamp, which provides a non uniform light source, with a specific intensity distribution. This emulates a random ambient condition of a non uniform light source falling on the surface of the earth.

However a systematic error that occurs is caused by the fact that the halogen lamp is a nearly punctiform light source, whereas the light from the sun, impinges parallel upon the surface of the earth.

Figure 4.12.
$I_{E,P}/I_{E,L}$ for $r = 220\,\mathrm{mm}$
and $w = 57\,\mathrm{mm}$.

One systematic error, caused by this, distorts the dependance $I_E(\nu)$, where I_E is the incoming energy flux. It is illustrated on the right side of figure 4.13. For a parallel light source $I_{E,L}(\nu) = I_{E,0} \cdot \cos(\nu) = I_{E,0} \cdot (w'/w)$ is valid, where $I_{E,L}(\nu)$ is the dependance with ν for a parallel lightsoure and $I_{E,0}$ is the incoming energy flux at $\nu = 0$.

However for a punctiform lightsource $I_{E,P}(\nu) = I_{E,0} \cdot (\alpha_2/\alpha_1)$ is valid. By applying angular functions to the schematic on the right side of figure 4.13 we get:
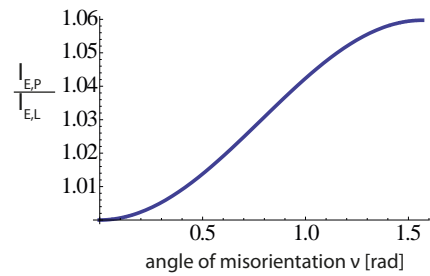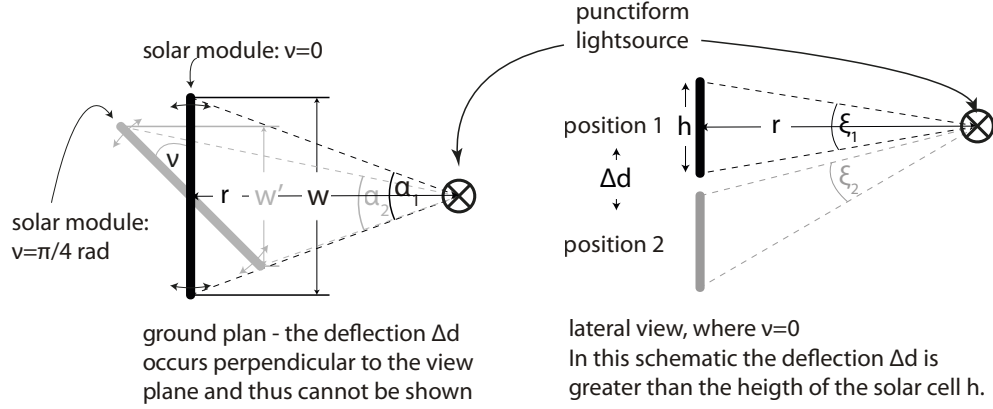
Figure 4.13.
Possible systematic errors that might occur from the fact, that the light source is punctiform.

$$\alpha_2 = \arctan\left(\frac{(w/2)\cdot\cos(\nu)}{r - (w/2)\cdot\sin(\nu)}\right) + \arctan\left(\frac{(w/2)\cdot\cos(\nu)}{r + (w/2)\cdot\sin(\nu)}\right) \qquad (4.9)$$

The distance between the halogen lamp and the solar cell r is $220\,\text{mm}$ and the width w of the solar module equals $57\,\text{mm}$ as mentioned in section 4.1.1. The results for $I_{E,P}/I_{E,L}$ have been plotted in Mathematica [27] and are shown in figure 4.12. For a misorientation angle ν of exactly $\pi/2\,\text{rad}$ the function $I_{E,P}/I_{E,L}$ is undefined since the incoming energy flux is 0 for $I_{E,P}$ and $I_{E,L}$. However for $\nu \to \pi/2$ the error amounts to $6\,\%$. This only affects $I_E(\nu)$ and thus not the fraction of the superimposed a.c. component.

Another systematical error is illustrated on the right side of figure 4.13. For a homogenous light source, impinging parallely on the solar module, the deflection Δd would have no impact on the incoming light flux of the solar cell. However for a punctiform homogenous light source this results in a change of the angle diameter ξ_s, covered by the solar cell. In theory or for very large displacements Δd, this would lead to an additional error. In our case $r = 220\,\text{mm}$ and $\Delta d = 4.25\,\text{mm}$. This leads to a systematic error of roughly $4.25/220 = 2\%$ of the magnitude of the superimposed a.c. signal.

4.4.2. Photons entering a solar cell

We want to obtain the maximum solid angle $\Omega_{max,medium}$ in which photons enter the doped layers of a solar cell as shown in figure 2.4. Thus we can determine how the optical path length a photon can travel, before it arrives at the backside of

the solar cell, depends on the angle of incidence of the incoming light. To obtain this angle we need the index of refraction, of the base material of the solar cell.

The index of refraction for the anti-reflection coating or any translucent material between the doped layers of the solar cell and the ambient air n_2 is not relevant for this analysis, as we can see by applying Snell's law:

$$n_1 \sin \alpha_1 = n_0 \sin \alpha_0 = n_2 \sin \alpha_2 \qquad (4.10)$$

Where n_0 is the refractive index of the anti-reflection coating, n_1 is the refractive index of the ambient air, n_2 is the refractive index of the solar cell and each α is the associated angle of light of the respective medium measured from the surface vector of the solar cell.

The band gap of silicon at RT is roughly $1.1\,\text{eV}$ [24, p. 36], the band gap of a-Si varies but is usually about $1.7\,\text{eV}$ [24, p. 217]. To obtain the corresponding wavelength we can use the formula $E(\text{eV}) \cong \frac{1240\,\text{nm}\cdot\text{eV}}{\lambda\,\text{nm}}$. For the band gap of a-Si we derive $\lambda = 730\,\text{nm}$ and for bulk silicon $\lambda = 1127\,\text{nm}$. At this wavelength the associated refractive index n for bulk silicon is 3.56 with shorter wavelenghts it further increases to 3.77 for $700\,\text{nm}$ and to 5.50 for $400\,\text{nm}$ [12].

The refraction index of amorphous silicon for the corresponding wavelength is $n = 4.25$ [4] and peaks at $\lambda = 430\,\text{nm}$ with $n = 5.18$, before it declines again for higher energies.

The refraction index of air is roughly 1. We are using Snell's law for the angle of total internal reflection:

$$n_1 \sin \alpha_1 = n_2 \sin \alpha_2 \qquad (4.11)$$

With $n_1 = 1$ we obtain:

$$\sin \alpha_{total} = 1/n_2 \qquad (4.12)$$

For photons, able to excite an electron to the conduction band for bulk silicon we get for the angle of total reflection: $\alpha_{tot,Si} = 0.28\,\text{rad}$ (16.3°). For a-Si we get $\alpha_{tot,a-Si} = 0.24\,\text{rad}$ (13,5°).

Hence it is of very minor importance from which angle a photon hits the solar cell. For a constant thickness of the solar cell, the absorbed intensity remains nearly constant, no matter from which angle a photon impinges.

4.4.3. Measurements and results

The measurement was carried through with the amorphous silicon miniature module. The angle ν was varied as can be seen in figure 4.11. The solar module was
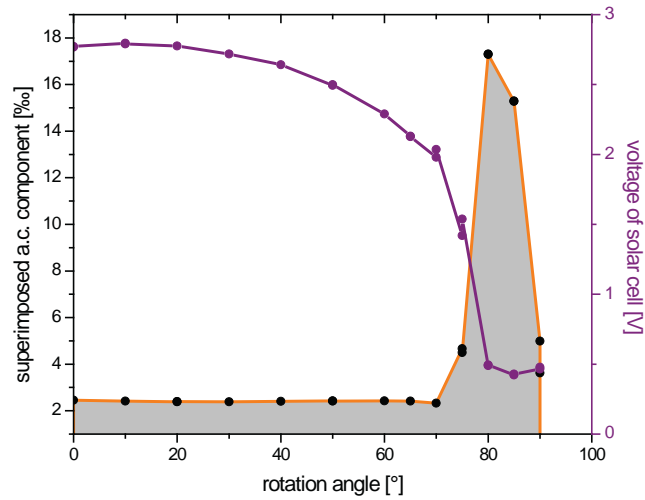
i

Figure 4.14.
Variation of angle ν for the amorphous silicon cell.

operated with a $1\,\mathrm{k\Omega}$ resistor. The excitation frequency was $8.68\,\mathrm{Hz}$ which corresponds to a deflection of $4.3\,\mathrm{mm}$ and its time constant of the lock-in amplifier was set to the maximum of $100\,\mathrm{s}$.

The drop of the voltage in dependance of the rotation angle ν, resembles eq. 4.9 or a cosine function (see section 4.4.1). The maximum of the superimposed a.c. component is nearly $19\,\permil$ of the d.c. output of the solar cell but doesn't exceed $3\,\permil$ from up until an angle of $\psi = 70°$. This unusually high a.c. component is most likely a result of the glass front of the a-si cell. The silicon layer is deposited on $4\,\mathrm{mm}$ thick transparent glass. Since the solar cell is not encapsuled in a module, light impinging on the solar cell sideways can enter the glass. When most of the light impinges sideways, small variations of the inhomogeneous light source can cause remarkable changes to the resulting power output of the solar cell.

5. Electronic Simulation

In this chapter a simulation in Qucs [3] was carried through, to support the interpretation of the measurement results obtained in chapter 4. Specifically the behavior of two solar cells, connected either in series or parallel, an the ensuing propagation of the transient a.c. noise was simulated.

5.1. Basic parameters

The solar cell was emulated with an equivalent circuit diagram in its most basic form, consisting of a shunt resistance R_{SH}, a series resistance R_S, a diode and a current source, as explained in section 2.5.2.

In the laboratory setup the modulation of the incoming light intensity happened through a modulation of the position of the solar cell. A shift in the position of the incoming inhomogeneous light, or partly shadowing the solar cell, yields the same results in the very low frequency regime. In the simulation the change of the incoming light intensity was emulated by a second sinusoidally altering current source, connected in parallel to the direct current source, usually known from PV-models. A schematic circuit diagram of the simulation, where the two cells are connected in series is shown in figure 5.1. The main parameters of the simulation are shown in table 5.1.

All measurements where carried through with a frequency of $10\,\mathrm{Hz}$ for the altering current source I_{AC}. The ratio of I_{AC} to I_{DC} was defined by $\Delta I_{AC,max} = 0.1 \cdot I_{DC}$,

Parameter	Cell #1	Cell #2
Diode factor n	2	2
Saturation current I_0	$0.93\,\mu\mathrm{A}$	$0.655\,\mu\mathrm{A}$
Series resistance R_S	$0.303\,\Omega$	$5.09\,\Omega$
Shunt resistance R_{SH}	$5.55\,\mathrm{k}\Omega$	$0.312\,\mathrm{k}\Omega$
Photo current I_L	$18.6\,\mathrm{mA}$	$28.5\,\mathrm{mA}$
Load Resistance R_{load}	$1\,\Omega - 1\,\mathrm{k}\Omega$	$1\,\Omega - 1\,\mathrm{k}\Omega$

Table 5.1.
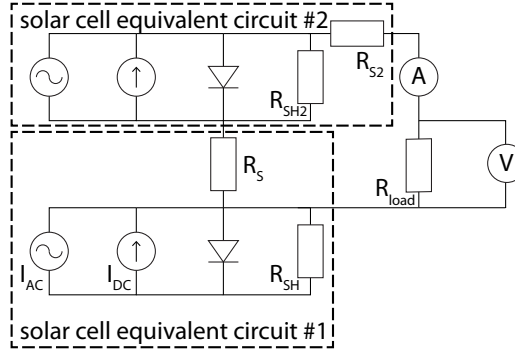Main parameters of the simulation.

Figure 5.1.
Qucs Setup for the simulation of two solar cells connected in series.

which represents a very dominant noise source. For each load resistance R_{Load} a transient simulation was executed for 200 ms, thus two full cycles could be covered. A visualization of the derived data, for the a.c. voltage signal at R_{load}, is shown in figure 5.2. It was recorded during a run with the solar cells connected in series as shown in figure 5.1. R_{Load} was increased logarithmically, starting at 1 Ω and going up to 500 Ω.

5.2. Transfer function

In the experimental setup the most common arrangement was to use a lock-in amplifier to measure the a.c. share of the resulting signal. However a lock-in amplifier is defined by having a very narrow bandwidth. This, in combination with the fact that the lock-in amplifier measures the voltage, while the fluctuations of the incoming light affect the current, leads to an additional error.

The bandwidth B of a lock-in amplifier is defined by the time constant τ [14]:

$$B = \frac{1}{4\tau} \tag{5.1}$$

For the low frequency regime a long time constant is inevitable, which leads to a very narrow bandwidth. Assuming a time constant of 100 seconds (which was used in most of our measurements) results in a bandwidth of $1/400$ or $0.025\,\text{Hz}$, which is very narrow with the given excitation frequencies being about 10 Hz.

While the incoming light flux is proportional to the current I, the output is measured in volt. The relation between current simulation and the resulting voltage modulation is determined through the characteristic curve, which can only be approximated linearly in a very limited range. Therefore, in the range of
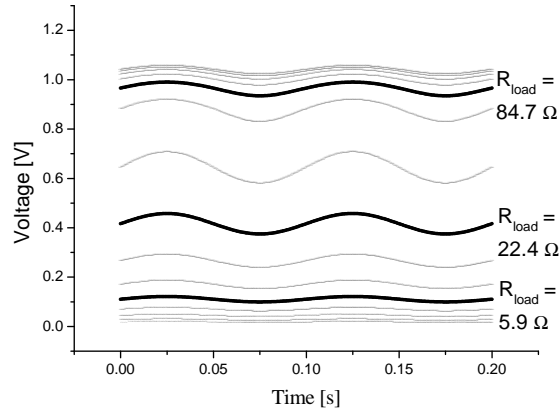
Figure 5.2.
Visualization of the a.c. part of the voltage at R_{load} from a simulation run.

strong non-linearity or very high current amplitudes the signal as a function of time gets distorted.

So even for a well defined sine signal as input, the frequency spectrum of the output signal will be more broadband, thus reducing the amplitude of the fundamental frequency. Hence any measurement with that experimental setup will be distorted, with the lock-in amplifier only being able to work with a very narrow bandwidth. Additionally it is very likely that the distortion produces some harmonic higher frequency amplitudes, which further decreases the amplitude of the base frequency. Figure 5.3 shows a schematic of the transfer function. The $x(t)$ depiction of the excitating altering current corresponds to a sine curve, whereas in the resulting altering voltage significant distortion occurs. The characteristic curve in the figure is derived from our two simulated solar cells connected in parallel. The inset shows an exemplary result of the amplitude spectrum of the resulting voltage curve.

5.3. Numerical differentiation of $\Delta V/\Delta R$

For further analysis it is useful to discuss, how well the numerical differentiation $\Delta V/\Delta R$ matches the amplitude of the fundamental frequency of the altering current, at the output. To accomplish this a single cell was tested with the specifications given above ($f = 10\,\mathrm{Hz}$, $\Delta I_{AC,max} = 0.1 \cdot I_{DC}$). The resulting output signal was FFT transformed to obtain the amplitude of the first harmonic of the altering voltage and is shown as the orange line in figure 5.4. The result was multiplied by 10 to fit well with the voltage axis on the right hand side.
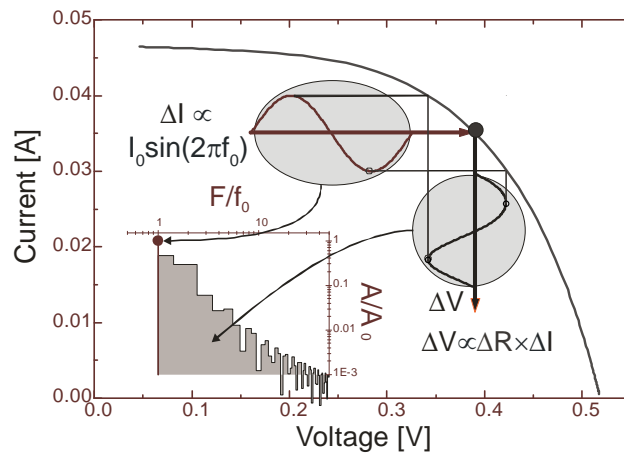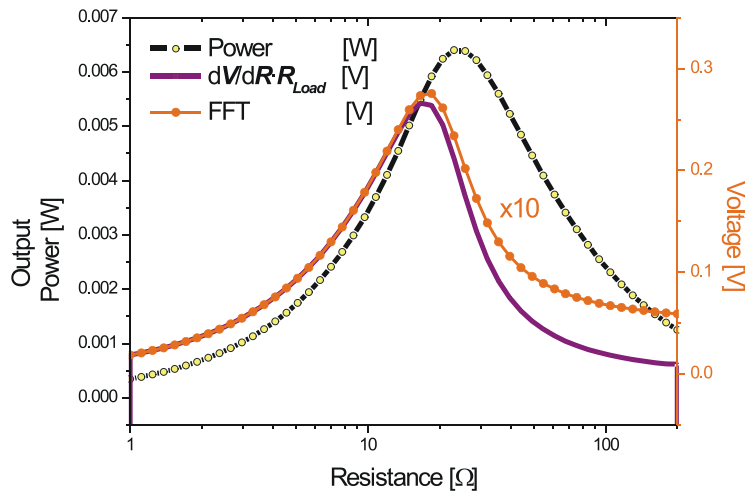
Figure 5.3.
Transfer function between modulated current and resulting voltage signal. In the lower left corner a power spectrum, derived from a circuit simulation illustrates the problem.

5.4

Figure 5.4.
Comparison of the transfer function derived from the characteristic curve and from the amplitudes derived through FFT at the excitation frequency.

Additionally the numerical differentiation $\Delta V/\Delta R$ was calculated and multiplied with R_{Load}.

For small load resistances and respectively small voltages the two curves correspond pretty well. The transfer function in this region is linear because it is determined by the shunt resistance R_{SH}, which results in nearly no distortion at the output signal. For higher load resistances corresponding to a higher d.c. voltage V_{DC} the exponential characteristic of the diode becomes noticeable. Alternating and direct current both vary strongly with the d.c. voltage V_{DC} and the external load resistance R_{Load}.

Additionally the power was calculated and is shown in figure 5.4. The fact that the maximum of the distortion signal with regard to the load resistance R_{Load} or the d.c. voltage V_{DC} is below the maximum power point is a little surprising, since one would intuitively assume that they would concur. This result is also confirmed for the simulation carried through for different circuit arrangements in the next section. However it could neither be confirmed nor falsified by the experimental setup.

5.4. Simulation for a parallel and a series connected setup

In figure 5.5 the result of the simulation of a series circuit (left hand diagram) and a parallel circuit (right hand diagram) are juxtaposed. Both simulations were executed with identical parameters, lest the interconnection. Characteristic current voltage curves (i.e. the black line, scaled according to the left hand side y-axis) and the power curve (i.e. the filled curve, scaled according to the left hand side y-axis) were derived from the direct current simulation. The $I(R_{Load})$ curve was used to differentiate $\Delta V/\Delta R$. The result was multiplied with R_{load} and is represented as dotted line with the corresponding right hand side y-axis scaling (as in the previous section). The transient simulation was carried out for a time interval of $200\,\mathrm{ms}$ (two periods for $f = 10\,\mathrm{Hz}$) yielding 11 pairs of variates of averages of V_{mean} and I_{mean} which are plotted as empty circles over the characteristic curves. The a.c. component of the signal was FFT transformed and evaluated according to the amplitude of the base frequency (i.e. the filled diamond symbols, scaled according to the right hand side y-axis). For both simulations the a.c. amplitudes accord sufficiently well with the differentiation of the characteristic curve of the direct current simulation, which suggests that only minor signal distortion takes place. However it can be seen that the maximum of the a.c. signal lies a little below the maximum power point of the characteristic $I(V)$ curve in relation to the voltage as also shown in the previous section for a single cell.

Figure 5.5.
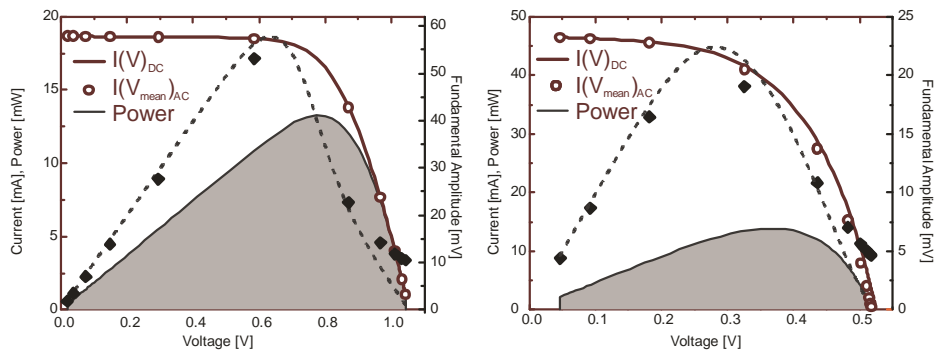Results of the simulation for a series connection (left hand side) and a parallel connection (right hand side) of the two cells. The keys for the curves scaled according to the left hand side y-axis are as inset in the graphic. The dashed line and the diamonds are scaled according to the right hand side. The first was derived via $R_{load} \cdot \Delta V/\Delta R$. The latter are the FFT of $V(t)$.

6. Conclusions

Vibration induced distortion is caused by the inhomogeneity of the incoming radiation and a displacement of the solar cell. The light impinging on a PV system can be divided into diffuse and direct contributions. For wind induced noise only the direct beam contribution is responsible. These results were verified by the experiments and the computer simulation.

In this work it has been tried to conduct a qualitative analysis of this effect, with special regard to the operating point, the circuit arrangement and the dependency of the angle of misorientation, between the surface vector of the solar cell and the vector pointing towards the sun.

The results are mainly confined to the specific setup and our photovoltaic units, however in most cases wind induced vibration will be the main contributor to a.c. distortions of the d.c. output, occurring below $100\,\mathrm{Hz}$.

To assess the impact of the distortion for different circuit arrangements, two cells have been connected either in series or parallel in the laboratory and in the computer simulation. In the simulation, for the cells connected in series the magnitude of the distortion was more than twice as large, as for the cells connected in parallel. In the laboratory experiments the series connection distortion was nearly ten times larger, which may have been due to our experimental setup. However it clearly showed that cells connected in parallel can mitigate the effect of wind induced distortion, even when compared to a single cell.

Qualitatively the computer simulation agrees with the experimental observation however, the simulation as well as the differentiated $\Delta V/\Delta R_{Load}$ d.c. curve suggest that the maximum of the distortion signal lies close to but below the maximum power point with regard to the load resistance. The laboratory results showed that the maximum distortion is very close to the MPP, however if it really lies below the MPP could neither be confirmed nor falsified.

The fraction of the magnitude of the noise voltage to the operating voltage never exceeded several per mill in the very specific laboratory setup. Additionally the results where obtained with a lock-in amplifier and a time constant of $100\,\mathrm{s}$, which inherently underestimates the magnitude of the full distortion. However during outdoor observations, where a solar module with 36 solar cells connected in series was used, the fraction regularly exceeded one per cent and could increase further once several conditions are met at the same time.

6. Conclusions

Outdoors the magnitude of oscillations depends on the mounting construction and will increase with increasing wind forces. Due to thermal management of photovoltaic collectors, construction design favors good ventilation conditions, which in return eases wind attacks. Thus vibration induced distortion appears to be unavoidable.

The outdoor measurements showed that low angles of misorientation of the solar module's surface vector towards the sun, can reduce the magnitude of the distortion. Additionally laboratory results indicate that the optical characteristics of the solar cell's or module's surface, can greatly amplify the noise ratio, especially when the angle of misorientation approaches $\pi/2\,\mathrm{rad}$.

Tracked systems will experience less distortion, since they are aimed at keeping the angle of misorientation low. For concentrating systems a separate analysis would be required, but since any shift out of the focus of the image forming system of the solar cells, would have a great effect, they probably are very susceptible to wind induced vibrational disturbances. Due to their large inclination angle facades are considerably misoriented towards the sun most of their operation time, which makes them prone to vibration induced distortion as well.

Bibliography

[1] http://www.pv-tech.org/news/nrel_confirms_world_record_43.5_
efficiency_on_solar_junctions_cpv_cell.

[2] *Global Market Outlook for Photovoltaics until 2015.* European Photovoltaic Industry Association.

[3] http://qucs.sourceforge.net/index.html.

[4] http://refractiveindex.info.

[5] Nabil A. Ahmed and Masafumi Miyatake. A novel maximum power point tracking for photovoltaic applications under partially shaded insolation conditions. *Electric Power Systems Research*, 78:777–784, 2008.

[6] Viorel Badescu. Simple optimization procedure for silicon-based solar cell interconnection in a series-parallel pv module. *Energy Conversion and Management*, 47:1146–1158, 2006.

[7] J. Bartlett, R.M. Margolis, and C.E. Jennings. Effects of the financial crisis on photovoltaics: An analysis of changes in market forecasts from 2008 to 2009. *National Renewable Energy Laboratory*, 29, 2009.

[8] M.H.J. Bollen and M. Häger. Power quality: Interactions between distributed energy resources, the grid, and other customers. *Eletrical Power Quality and Utilisation Magazine*, 1:51–61, 2005.

[9] M.H.J. Bollen, Y. Yang, and F. Hassan. Integration of distributed generation in the power system - a power quality approach. In *Harmonics and Quality of Power, 2008. ICHQP 2008. 13th International Conference on*, pages 1 –8, 28 2008-oct. 1 2008.

[10] G. Chicco, J. Schlabbach, and F. Spertino. Experimental assessment of the waveform distortion in grid-connected photovoltaic installations. *Solar Energy*, 83:1026–1039, 2009.

[11] M. Drapalik, V. Schlosser, J. Schmid, P. Bajons, and G. Klinger. Investigations of rf noise introduced by photovoltaic solar power generators. In *23rd European Photovoltaic Solar Energy Conference and Exhibition, 1-5 September 2008, Valencia, Spain*, pages 3367 – 3370, 2008.

[12] Martin A. Green and Mark J. Keevers. Optical properties of intrinsic silicon at 300 k. *Progress in Photovoltaics: Research and Applications*, 3:189–192, 1995.

Bibliography

[13] T. Hiyama and K. Kitabayashi. Neural network based estimation of maximum power generation from pv module using environmental information. *IEEE Transactions on Energy Conversion*, 12:241–246, 1997.

[14] Paul Horowitz and Winfield Hill. *The Art of Electronics*. Cambridge University Press, 1989.

[15] National Instruments. Labview 7.1.

[16] Ward T. Jewell and Timothy D. Unruh. Limits on cloud-induced fluctuation in photovoltaic generation. *IEEE Transactions on Energy Conversion*, 5:8–14, 1990.

[17] J.M.Enrique, E.Durán, M.Sidrach de Cardona, and J.M.Andújar. Theoretical assessment of the maximum power point tracking efficiency of photovoltaic facilities with different converter topologies. *Solar Energy*, 81, Issue 1:31–38, 2007.

[18] A.D. Jones and C.P. Underwood. A thermal model for photovoltaic systems. *Solar Energy*, 70:349–359, 2001.

[19] Tomas Markvart. *Solar Electricity*. University of Southampton UK, 1994.

[20] Fumitoshi Matsuno, Michinori Hatayama, Hideaki Senda, Tomoaki Ishibe, and Yoshiyuki Sakawa. Modeling and control of a flexible solar array paddle as a clamped-free-free-free rectangular plate. *Automatica (Journal of IFAC)*, 32:49 – 58, 1996.

[21] L. Moore, H. Post, H. Hayden, S. Canada, and D. Narang. Photovoltaic power plant experience at arizona public service: A 5-year assessment. *Progress in Photovoltaics: Research and Applications*, 13:353–363, 2005.

[22] L.M. Moore and H.N. Post. Five years of operating experience at a large, utility-scale photovoltaic generating plant. *Progress in Photovoltaics: Research and Applications*, 16:249–259, 2008.

[23] T. Muneer. *Solar Radiation and Daylight Models*. Elsevier Butterworth-Heinemann, Second edition 2004.

[24] Jenny Nelson. *The Physics of Solar Cells*. Imperial College Press 57 Shelton Street Covent Garden London WC2H 9HE, 2003.

[25] J.K. Page. The estimation of monthly mean values of daily short wave irradiation on vertical and inclined surfaces from sunshine records for latitudes 60° n to 40° s. *Proc. United Nations on New Sources of Energy*, 4:378–390, 1977.

[26] M.C. Di Piazza, C. Serporta, G. Tinè, and G. Vitale. Electromagnetic compatibility characterisation of the dc side in a low power photovoltaic plant. pages 672–677, 2004.

[27] Wolfram Resarch. Mathematica 6.1.

70

[28] J. Schmid, M. Drapalik, E. Kancsar, V. Schlosser, and G. Klinger. A study of power quality loss in pv modules caused by wind induced vibration located in vienna. *Solar Energy*, 85:1530 – 1536, 2011.

[29] J. Schmid, E. Kancsar, M. Drapalik, V. Schlosser, and G. Klinger. Investigations of the response of a photovoltaic power generator to mechanical vibrations. In *Jahrestagung der österreichisch physikalischen Gesellschaft 2008 (22.-26. Sep. 2008)*, 2008.

[30] J. Schmid, E. Kancsar, M. Drapalik, V. Schlosser, and G. Klinger. Investigations of the response of a photovoltaic power generator to mechanical vibrations. In *24th European Photovoltaic Solar Energy Conference*, pages 3301 – 3304, Hamburg, Germany, 2009.

[31] J. Schmid, E. Kancsar, M. Drapalik, V. Schlosser, and G. Klinger. Investigations of wind induced vibrations on the output current of photovoltaic solar modules. In *Jahrestagung der österreichisch physikalischen Gesellschaft 2009 (2.-4. Sep. 2009)*, Innsbruck, Austria, 2009.

[32] J. Schmid, E. Kancsar, M. Drapalik, V. Schlosser, and G. Klinger. A study of vibration induced distortion on the performance of photovoltaic converters. In *Power Electronics and Motion Control Conference (EPE/PEMC), 2010 14th International*, pages T12–21 – T12–27, 2010.

[33] William Shockley and Hans J.Queisser. Detailed balance limit of efficiency of p-n junction solar cells. *Journal of Applied Physics*, 32:510 –519, 1961.

[34] T. Trupke, M. A. Green, and P. Wurfel. Improving solar cell efficiencies by down-conversion of high-energy photons. *Journal of Applied Physics*, 92:1668–1674, 2002.

[35] J. Wieringa. Roughness-dependent geographical interpolation of surface wind speed averages. *Quarterly Journal - Royal Meteorological Society*, 112:867–889, 1986.

[36] Peter Würfel. *Physik der Solarzellen*. Spektrum Akademischer Verlag, 2000.

A. Addendum

A.1. Symbols

name	symbol	unit
life time	τ	s
length	L	m
angular frequency	ω	rad/s
temperature	T	K
distribution of photons with respect to their energy	f_r	none
momentum	p	$\text{kg} \cdot \text{m/s}$
volume	V	m^3
number of states	N	-
density of states per volume and energy interval	D	$(\text{J} \cdot \text{m}^3)^{-1}$
number of photons per volume	n_γ	m^{-3}
energy	E	J
energy of a photon	ϵ_γ	J
energy density per volume	e_γ	J/m^3
energy flux density	j_E	$\text{J} \cdot \text{s}^{-1} \cdot \text{m}^{-2}$
energy flux	I_E	$\text{J} \cdot \text{s}^{-1}$
area	A	m^2
solid angle	Ω	sr
refraction index	n	none
absorptivity	a	none
absorption coefficient	α	cm^{-1}
transmissivity	t	none
emissivity	ε	none
reflectivity	r	none
concentration ratio	C	none
generation rate	G_γ	$\text{m}^{-3}\text{s}^{-1}$
daily solar radiation (dose)	G	J/m^2
daily direct radiation (dose)	B	J/m^2
daily diffuse radiation (dose)	D	J/m^2
daily albedo radiation (dose)	R	J/m^2
attenuation of solar radiation	K_T	none
resistance	R	Ω
voltage	V	V

name	symbol	unit
current	I	A
power	P	W
duty cycle	δ_c	none
bandwidth	B	s^{-1}

A.2. Angles

angle	name	explained in section:	reference frame / keyword
Ω	solid angle [sr]	2.3.3	laboratory
β	no name	2.3.3	laboratory
ϕ	no name	2.3.3	laboratory
δ	solar declination	2.4.1	celestial sphere
θ_Z	zenith angle	2.4.2	observer
α	solar elevation	2.4.2	observer
τ	solar azimuth	2.4.2	observer
ω	hour angle	2.4.2	observer
ψ	geographical latitude	2.4.2	celestial sphere
κ	inclination of solar cell	2.4.5	observer
ψ	yaw angle	3.2	yaw-pitch-roll / observer
θ	pitch angle	3.2	yaw-pitch-roll / observer
φ	roll angle	3.2	yaw-pitch-roll / observer
α	no name	4.2	laboratory
β	no name	4.2	laboratory
γ	no name	4.2	laboratory
Φ	no name	4.2	laboratory
ξ	angle diameter	4.4	laboratory

A.3. Constants

name	symbol	value	units
Boltzmann constant	k	$1.3806488(13) \cdot 10^{-23}$	J/K
Planck constant	h	$6.62606957(29) \cdot 10^{-34}$	$\text{J} \cdot \text{s}$
reduced Planck constant	$\hbar$	$1.054571726(47) \cdot 10^{-34}$	$\text{J} \cdot \text{s}$
magnitude of elementary charge	q	$1.602176565(35) \cdot 10^{-19}$	C
speed of light in vacuum	c_0	299792458	m/s
solar constant	S	1367	W/m^2

B. curriculum vitae

Name:	Julian Schmid
Date of birth:	December 6$^{\text{th}}$, 1983
Place of birth:	Vienna, Austria

Diploma thesis:	Title
	Advisor: Viktor Schlosser

Oct. 2002 - present:	studies in Physics at the Faculty of Physics, University of Vienna
2010 - present	Lab assistent for the physics laboratory at Fachhochschule Technikum Wien
June 2002:	Matura (school leaving examination)
1994 - 2002:	Erich Fried Realgymnasium
1990 - 1994:	Volksschule Börsegasse

C. Abstract - English

A study of vibration induced distortion on the output current of photovoltaic solar modules

The constant growth of photovoltaic systems and the ongoing trend towards large scale grid connected PV plants, invokes new challenges in assuring power quality. Among the several noise sources, wind induced vibration has as yet been mainly ignored. Mechanical vibrations of a solar module mounting rack cause oscillations in the orientation of the module towards the sun. The resulting intensity oscillations of the incident light generate an a.c. current at the module's terminals.

This diploma thesis examines this effect qualitatively, with most of the results being restricted to the given experimental setup. However it was possible to roughly asses the order of magnitude of these disturbances and their possible impact on large grid connected photovoltaic plants.

Measurements have been executed in the laboratory by means of a vibration table and outdoors, where a solar panel was mounted at the roof top of the physics institute building in Vienna. There it was exposed to ambient conditions. Additionally a circuit simulation was carried through to confirm the aquired results.

Special attention has been paid to the relation of three variables with regard to the disturbances of the solar cell:

Firstly the operating point of the solar cell. Here the simulation results show that the maximum of the induced noise lies a little below but close to the maximum power point, with regard to the voltage or resistance. In the laboratory experiments the noise maximum also lay close to the MPP. The induced noise may become important during MPP tracking.

Secondly a parallel and a series circuit arrangement of two solar cells was examined in the laboratory and simulated, accounting for module and array wiring. Here the results unambiguously show that solar cells connected in parallel are much less prone to low frequency noise distortion, typical for wind induced vibration. However the general tendency in PV applications favours large series connections in order to increase the working voltage.

C. Abstract - English

Thirdly the angle dependency has been studied in the laboratory and outdoors. The results show that the proportion of vibration induced noise decreases with a low angle of misorientation. Additionally at very large angles, where the light source falls nearly perpendicular on the surface of the solar module, the optical characteristics of the casing of the module can lead to significant disturbances.

D. Abstract - German

Eine Untersuchung vibrationsinduzierter Störsignale auf die Ausgangsspannung photovoltaischer Solarmodule

Das konstante Wachstum von Photovoltaikanlagen und der ungebremste Trend hin zu großen netzgekoppelten Systemen, schaffen neue Herausforderungen, um Netzstabilität und Versorgungsstabilität (Power Quality) zu gewährleisten. Durch Wind hervorgerufene Vibrationen wurden unter den vielen möglichen Störquellen bis jetzt größtenteils ignoriert. Mechanische Vibrationen der Halterung eines Solarmoduls verursachen Schwankungen in der Ausrichtung des Moduls gegenüber der Sonne. Die resultierenden Intensitätsschwankungen erzeugen eine Wechselstromkomponente an den Anschlussklemmen der Solarzelle.

Diese Diplomarbeit untersucht diesen Effekt qualitativ, wobei die Resultate auf die spezifische Versuchsanordnung beschränkt bleiben. Trotzdem war es möglich die Größenordnung und deren möglichen Einfluss auf große netzgekoppelte Photovoltaikanlagen abzuschätzen.

Messungen wurden im Labor, mithilfe eines Vibrationstisches und im Freien durchgeführt. Dort wurde ein Solarmodul am Dach des Institutsgebäudes der Physik angebracht, wo es realen Umweltbedingungen ausgesetzt war. Zusätzlich wurde eine Schaltkreissimulation durchgeführt um die erhaltenen Resultate zu bestätigen.

Spezielle Aufmerksamkeit wurde auf drei Variable, in Abhängigkeit zu den Störsignalen der Solarzelle gerichtet:

Erstens dem Betriebspunkt der Solarzelle. Hier zeigen die Resultate der Simulation, dass das Maximum des induzierten Störsignals etwas unterhalb, in Bezug auf die Spannung und den Widerstand, des optimalen Betriebspunktes (*MPP*) liegt. In dem Labormessungen lag das Maximum des Störsignals ebenso nahe des optimalen Betriebspunktes. Diese Störsignale können bei MPP Trackern zu Problemen führen.

Zweitens wurde die Serien- und Parallelschaltung von zwei Solarzellen simuliert und im Labor untersucht. Hier zeigen die Resultate eindeutig, dass parallel geschaltene Solarzellen weit weniger anfällig für Niedrigfrequenzstörungen sind. Der

allgemeine Trend geht jedoch hin zu großen Serienschaltungen, um die Arbeitsspannung zu erhöhen.

Drittens wurde die Winkelabhängigkeit im Labor und im Freien untersucht. Die Resultate zeigen, dass der Anteil von durch Vibrationen verursachten Störsignalen mit sinkender Fehlorientierung zur Sonne zurückgeht. Zusätzlich kann die optische Charakteristik der Verschalung des Moduls zu signifikanten Störungen führen, wenn das Licht in einem sehr flachen Winkel auf die Oberfläche der Solarzelle fällt.